Synthetic Aperture Beamforming in Ultrasound using Moving Arrays.

Andresen, Henrik Stenby; Nikolov, Svetoslav; Jensen, Jørgen Arendt

Publication date:
2009

Document Version
Publisher's PDF, also known as Version of record

Synthetic Aperture Beamforming in Ultrasound using Moving Arrays.

Henrik Andresen

May, 2009

B-K Medical, Denmark &
Center for Fast Ultrasound Imaging, CFU
Technical University of Denmark

SUBMITTED IN PARTIAL FULFILLMENT OF THE
REQUIREMENTS FOR THE DEGREE OF
DOCTOR OF PHILOSOPHY
AT
THE TECHNICAL UNIVERSITY OF DENMARK
APRIL 2009

Signature of Author

Contents

CHAPTER

ONE

Introduction

Medical ultrasound (US) is widely used because it allows cheap real-time imaging of soft tissue with no known side-effects or hazards to either patients or operating personnel. US has existed since the 1960s and was originally adapted from the concept of radar and sonar. The development in ultrasound has allowed the technology to evolve from a showing a simple echo along a line to fully visualize entire organs.

The image changes significantly depending on the orientation of the transducer, making it more difficult to see exact features. This poses challenges since anatomy is three-dimensional and the limited view makes diagnosis of pathology difficult [1]. A full 3D volume acquisition makes it possible to capture larger areas at once, and also allows complete freedom in choosing the slice to view after the scan has been completed. This removes the need for doing additional scans if a significant slice was missed and allows a more precise measurement of organ dimensions [2, 3, 4].

Conventional 3D ultrasound imaging is basically faced with two limitations. It is only able to have a single transmit focus point and each line in a 3D volume has to be created independently. This reduces image quality outside the focus point and reduces temporal resolution. For better image quality it is desirable to achieve a good resolution at a large range of depths, and achieving a volume-rate fast enough to visualize the dynamics of the investigated organ.

A method showing the possibility of meeting both these challenges is synthetic aperture focusing (SAF). A full dynamic focusing is possible in both transmit and receive as well as the possibility of imaging an entire volume with only a few emission. The resolution of the resulting volume can be improved by using more emissions, giving a trade-off between temporal and spatial resolution. A challenge with SAF is a large increase in processing requirements, especially for 3D systems.

Ideally the method is able to achieve a good image quality for all depths in the volume with a time-resolution fast enough for cardiac images. This will allow better diagnoses with fewer scans, making each investigation less user-dependent. In the end this has the potential of reducing costs for each investigation, as both time required to scan, and the expertise needed to do so successfully can be reduced.

1.1 Three-Dimensional Ultrasound

Transducers used for 3D imaging can be divided into two groups. Moving 1D arrays and 2D matrix arrays. The moving 1D arrays are based on many years of knowledge in 2D imaging

and are well understood in regards to materials and production. A volume scan is done by imaging a series of planes and stacking these planes into a 3D volume. Placing a 1D array on a moving frame allows for a cheap way of achieving 3D imaging. Full 2D arrays have an extra dimension of elements, which means that a simple 64-element transducer has 4096 elements if the performance is identical both laterally and in elevation. The increased number of elements allows the transducer to steer the beam electronically in all directions, giving a large degree of freedom. On the downside, the many elements either have to be sparsely connected, or the receiving system has to be able to sample a large amount of data [5].

Acquiring a full volume presents other challenges depending on the acquisition system. A moving 1D array is often limited in frame rate by the mechanical system moving the transducer. Two-dimensional transducers are only limited by the scan depth and speed of sound. Since the required number of lines in a volume will also square, compared to a 2D image, the resulting volume rate will decrease significantly. A possible solution is proposed in [6] where several receive beams are created for each transmit. This allows for full real-time imaging of a selected volume with a volume rate exceeding 30 volumes/s.

Having a 3D data set poses another problem with visualizing the data. Other imaging modalities, like x-ray CT, use both slice imaging and 3D rendering with windows to isolate tissue. Ultrasound does not benefit from fixed values and the speckle nature of tissue makes windowing difficult. Often 3D volumes are visualized using orthogonal planes, which render a slice of the volume. Alternatively it is possible to use volume rendering methods for a more complete view [7]. Rendering is used in a limited area of ultrasound, which specializes in facial imaging of unborn babies.

1.2 Synthetic Aperture Focusing

A fundamental change between conventional ultrasound focusing and SAF is the ability to change the transmit and receive focus using post-processing. The idea originates from radar technology and has later been adopted for US imaging [8, 9, 10, 11].

The basic method assumes a single element is transmitting a spherical wave in all directions. To focus for any give point the transmit time-of-flight (ToF) is the direct path from the transmitting element to the point of interest. The receive ToF is similarly calculated as the direct path from the point of interest to the receiving element. This is shown in Fig. 1.1. The equation for calculating the delay value for a given point is

$$t_{\text{ToF}}(\vec{r}_p, m, n) = \frac{1}{c}\left(|\vec{r}_p - \vec{r}_m| + |\vec{r}_p - \vec{r}_n|\right) \quad , \tag{1.1}$$

where c is the speed of sound, m and n are the indices of the transmitting and receiving element, respectively, $\vec{r}_p$ is the position of the point of interest, $\vec{r}_m$ is the position of the transmitting element and $\vec{r}_n$ is the position of the receiving element. A full image can be beamformed with a single emission using (1.1) but will have a very low resolution due to the lack of transmit focusing. The image created from a single emission is often denoted as low-resolution images (LRI). By changing the position of the transmitting element a series of LRIs can be created, and a transmit focus can be obtained by summing all the LRIs into a high-resolution image (HRI). The process is visualized in Fig. 1.2. The entire summation for each point in the HRI is given

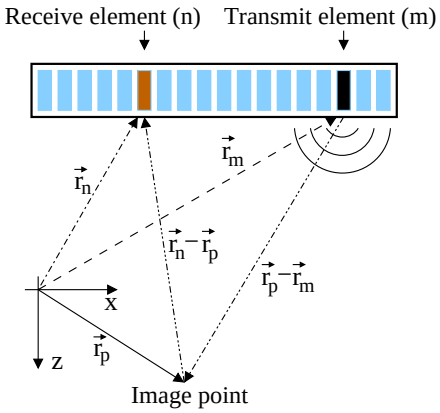

Figure 1.1: Synthetic aperture focusing calculated for a single point. Reproduced from [12].

by

$$s(\vec{r}_p) = \sum_{m=1}^{M} \sum_{n=1}^{N} a_{m,n} s_{m,n}(t_{\text{ToF}}(\vec{r}_p, m, n)) \quad , \tag{1.2}$$

where M is the number of transmitting elements, N is the number of receiving elements, $a_{m,n}$ and $s_{m,n}(t)$ is the apodization and complex envelope detected signal from the n^{th} element for the m^{th} emissions at time t, respectively. The use of SAF for array transducers has been done extensively with different geometries and uses [14, 15, 16, 17]. If only a single element is used in receive, and the transmit position is identical to the receive position, the method is known as the monostatic approach [18, 19]. This is mostly used for either simple systems with limited

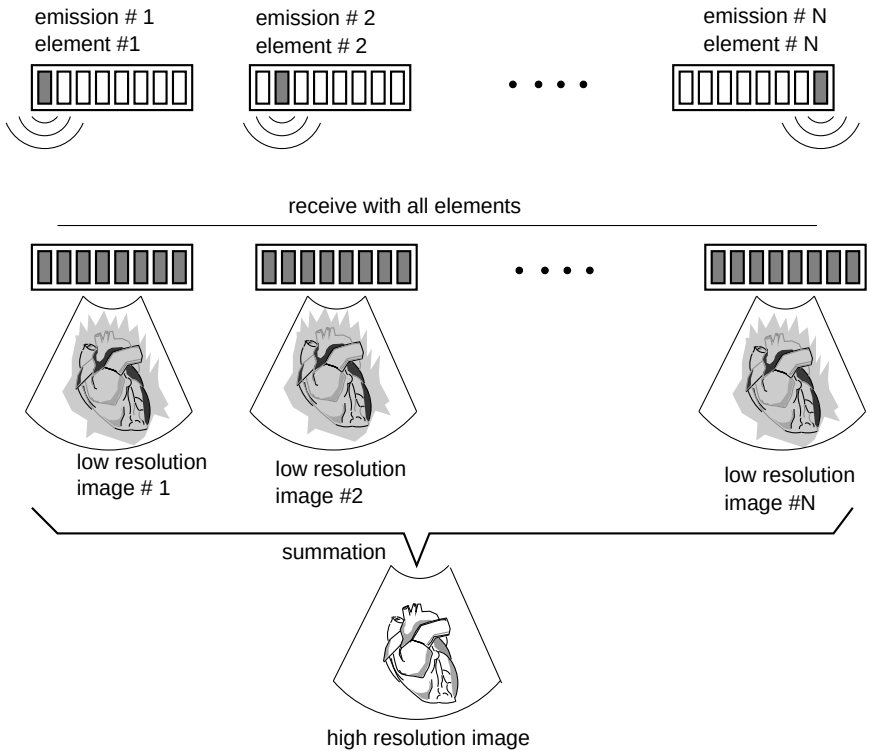

Figure 1.2: General structure of an SA image aquisition and beamforming. Taken from [13].

sampling capability or for single element transducers. In addition to imaging, several advances in flow estimation has been done using SAF [20, 21, 22]

1.2.1 Virtual Sources

Initial SAF systems assume a single element transmitted a spherical wave. This assumption has several disadvantages if implemented directly for array or single element transducers. Using a single array element limits the energy emitted due to the small size of each element. Increasing the element size by applying the same waveform to several elements breaks the assumption of a spherical wave emission. For a single element transducer with a large aperture, the assumption of a spherical emission gives a poor approximation to the actual wave-field, especially in the presence of a focusing lens.

A common framework is used, which allows for multi-element array emissions and a correct time-of-flight (ToF) expression for single element transducers with a focusing lens. A virtual source (VS) is introduced, to calculate the ToF, instead of using the position of the transmitting element [13, 23]. The VS is placed above or below the transducer surface, depending on whether a focused or de-focused emission is used.

Acceptance Angle

A common property of virtual sources is their acceptance angle. The angle defines a boundary, within which the assumption of spherical propagation is valid. Using a virtual source limits the part of the image that a given emission can contribute to, which also sets a limit to the final resolution. A geometric boundary approximation of this angle is shown in Fig. 1.3 and 1.4 for a focused and de-focused VS. This is in [24] shown to be a valid approximation and the angle is given by

$$\theta_a = \tan^{-1}\left(\frac{1}{2F\#}\right), \tag{1.3}$$

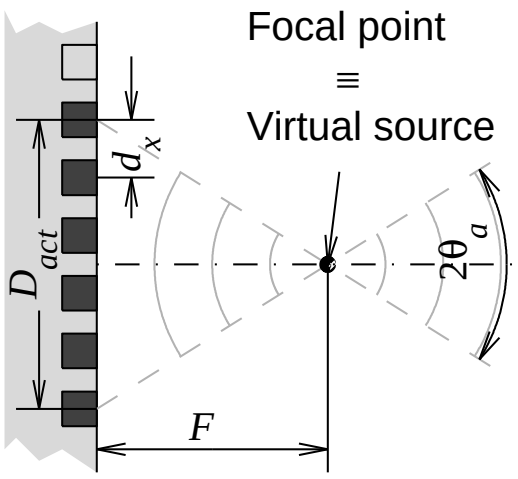

Figure 1.3: Visualization of a focused virtual source. Reproduced from [23].

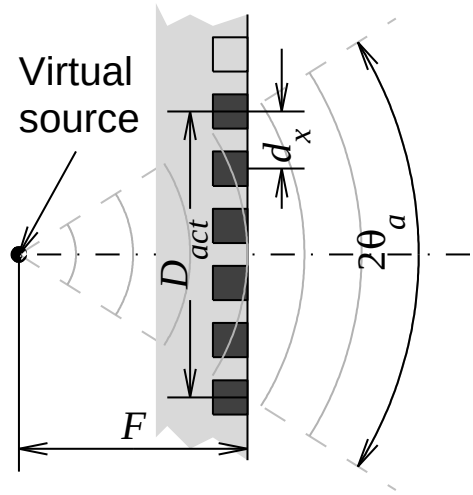

Figure 1.4: Visualization of a de-focused virtual source. Reproduced from [23].

where the $F^{\#} = \frac{F}{D_{\text{act}}}$ like conventional imaging, except the focusing depth is set to be the depth of the VS. The maximum $F^{\#}$ that can be attained using SAF utilizing VSs will be equal to the $F^{\#}$ of the VS, giving a lateral resolution, which can be approximated by $F^{\#}\lambda$.

The $F^{\#}$ for conventional transducers is defined to give a good resolution at the depth of interest, making the beam profile as narrow as possible. For SAF the $F^{\#}$ is desired to be as low as possible, to allow more emissions to contribute to the focusing, which is often opposite the design. This makes for an inherent problem when designing physical transducers for both conventional and synthetic aperture beamforming.

Multi Element Virtual Source Emission

To improve on the low SNR for an array transducer, several elements can be used in a single emission instead of only one. Each sub-element is delayed to mimic the propagation of a spherical wave originating from the virtual source position. The method is the same whether the VS is placed behind or in front of the transducer and is shown for both cases in Fig. 1.3 and 1.4. The multiple elements increase the emitted energy and as a result increase the SNR. The increase in SNR by using the VS approach is discussed further in [24, 25]. Multi element VS emission are widely used and have amongst other groups been used by [26, 27, 28].

Introducing a virtual source requires a modification to (1.1). The VS only influence the transmit propagation, leaving the receive ToF unchanged. The total ToF using a multi-element transmit VS is given by

$$t_{\text{ToF,ME}}(\vec{r}_p, m, n) = \frac{(|\vec{r}_p - \vec{r}_{\text{VS}}| \cdot \text{sign}(r_{p,z} - r_{\text{VS},z}) + r_{\text{VS},z} + |\vec{r}_p - \vec{r}_n|)}{c} \quad , \tag{1.4}$$

where $r_{p,z}$ is the depth of the point of interest, $\vec{r}_{\text{VS}}$ is the VS position, and $r_{\text{VS},z}$ is the depth of the virtual source. The lateral position of the VS is often placed at the center of the active elements. The delay profile of the sub-elements is calculated from

$$\Delta T_m = \frac{|\vec{r}_m - \vec{r}_{\text{VS}}| - r_{\text{VS},z}}{c}, \tag{1.5}$$

where c is the speed of sound, and $\vec{r}_m$ is the position of the m^{th} transmitting element.

Single Element Virtual Source

For a single element transducer the VS is placed at the focal point as shown in Fig. 1.3, except the focus is generated from a continuous aperture and not an array of elements. Using this approach allows several single element emissions to be combined outside the focal point of the transducer, which can improve the otherwise poor performance of a single element transducer, and has been used by several groups [29, 30].

A single element transducer has a focus defined by a physical lens. This lens changes the propagation in both transmit and receive instead of only in transmit as for an array emission. The total ToF can be calculated by twice the one-way ToF, and is given by

$$t_{\text{ToF,SE}}(\vec{r}_p) = \frac{2}{c}\left(|\vec{r}_p - \vec{r}_{\text{VS}}| \cdot \text{sign}(r_{p,z} - r_{\text{VS},z}) + r_{\text{VS},z}\right) \tag{1.6}$$

1.2.2 Effective Aperture

The acquisition time in SAF is limited by the imaging depth and the number of elements used. To achieve a focusing equal to that possible with conventional imaging, it is required to have the same effective aperture (EA) [31]. If all transmit elements used in the conventional imaging is used in turn in an SAF sequence, both imaging methods will have the same EA at the focal point, assuming the receive elements and apodization is the same. The EA is related to the the lateral resolution by the Fourier transform in both the far field and at the focal point. The continuous wave radiation pattern $P(s)$ is in [31] given by

$$P(s) = \mathcal{F}\left[a_T\left(\frac{x}{\lambda}\right) \otimes a_R\left(\frac{x}{\lambda}\right)\right] \quad , \tag{1.7}$$

where s is the direction sine of the angle, a_T is the transmit apodization function, a_R is the receive apodization function, $\left(\frac{x}{\lambda}\right)$ is the element location in wavelengths, and $\mathcal{F}[\cdot]$ is the Fourier transform.

From (1.7) it is seen the effective aperture is given from the convolution of the transmit and the receive aperture. For SAF the effective aperture of a single emission is roughly half the size of a conventional US image; hence the name for the beamformed image of a single emission is a low resolution image. When all the low resolution images are summed, so are the effective apertures, resulting in identical effective apertures for SAF and conventional imaging at the focal point. The technique is applied for aperture optimizations by several groups [5, 32, 33].

Applying the effective aperture principle in both 2D and 3D imaging is greatly dependent on the system. For a 2D transducer the benefits can be a sparse connection without large grating lobes. Moving array systems are often limited in the amount of time they spend in one area, and here it is desired to attain a smooth EA to obtain a well behaved point spread function (PSF).

1.2.3 Processing requirements

Dynamic transmit and receive focusing are possible because a full image is beamformed for each emission, which increases demands on the data processing. For conventional ultrasound the number of required ToF calculations per image is equal to

$$N_{\text{conv}} = N_r N_l N_p, \tag{1.8}$$

where N_l is the number of lines in each image, N_r is the number of receive elements used, and N_p is the number of points per line. For SAF this number is increased to

$$N_{\text{saf}} = N_e N_r N_l N_p = N_e N_{\text{conv}}, \tag{1.9}$$

where N_e is the number of emissions for a given image. Comparison of (1.8) and (1.9) shows an increase by a factor of N_e number of calculations. In addition to the required calculations an increased amount of data has to be moved since a full image is generated from each emission and not only a single line. The additional processing performed by the system becomes higher when moving to 3D imaging. If the number of lines and emissions increases by the square of the original, so does the increase in calculation requirements. Using 64 elements in transmit for the 2D case increases the computational cost by a factor of 4096 if using a 2D aperture for 3D imaging.

This increase in calculations has led to the development of two-step methods, which try to reduce the number of calculations, but still retain the resolution increase from SAF [34, 35]. Both methods can reduce the number of needed calculations, but require an intermediate storage between the two steps. In addition requirements on the interpolation for the second has to be adequate to retain low side-lobes [36].

1.2.4 Applying Synthetic Aperture Focusing

1.3 Purpose of the project

The application of SAF to 3D ultrasound imaging has the potential to improve on image resolution and reduce the needed time to acquire a full volume image. SAF combines data from several emissions for the same imaging points, which requires sampling of large amounts of RF-data over an entire volume. At the Center for Fast Ultrasound Imaging (CFU) the experimental scanner system RASMUS is capable of sampling 64 channels continuously for at least 3 seconds [37].

This PhD project will focus on acquiring volume data with moving 1D arrays. They are not as optimal as a full 2D array, but are much cheaper to acquire and single channel data can be acquired with the current systems. One-dimensional arrays are also desirable for actual implementation, since the lower system requirements will allow SAF to be realized commercially in the near future. Using a 1D array allows full SAF to be applied in the scan-plane of the transducer. In the elevation direction the improvements are limited by the motion of the transducer as well as the transducer geometry. Whether transducers move linearly or are rotating makes a big difference on the possible gain that can be achieved. A drawback with using commercial arrays for 3D SAF is that they are designed for imaging only a single plane. This has a big effect on the elevation focus, which is desired to be limited in conventional imaging, but limits the ability of SAF to improve on elevation resolution.

Implementing SAF for 3D imaging presents several challenges. The large processing requirements is a significant obstacle to implementing SAF in commercial systems. The beamforming of 3D datasets are limited to two basic ways of doing it. A direct approach where the ToF is calculated in 3D or a step wise approach where SAF is applied to one dimension at a time. This PhD project has focused on the processing requirements and possibilities with both approaches, and the effects and challenges with applying these.

In addition to the beamforming, the actual improvement possible with moving 1D arrays is investigated. A moving convex array as well as a single element transducer has been used for this purpose. The results from the single element transducer can easily be related to other moving array geometries, both rotating linear arrays, and translating circular arrays.

1.4 Structure of the Thesis

The thesis is divided into a series of chapters, where each chapter contains a presentation of the results gained in a journal paper. Following the presentation of results is a conclusion and a perspective of future research.

Chapter 2 introduces a new method for calculating the time-of-flight (ToF) for linear arrays in

three dimensions. This allows a new direct approach for beamforming in addition to the established two-step approach. The results show a slight improvement in ToF calculations compared to conventional beamforming, but also allows a reduced processing requirement if only a few planes are beamformed. This allows a real-time implementation using fewer resources. The chosen transducer is mounted on a moving arm, which allows carefull study of phantoms but is impractical for in-vivo measurements.

Chapter 3 investigates the potential of using SAF with a rocking convex array. The study shows the improvements gained in both simulations and phantom measurements as well as in-vivo. The in-vivo measurements show an improvement in elevation resolution, but also introduces some artifacts, which indicate that something unforeseen is happening. In addition to these results the effects of re-designed the transducer parameters for SAF is investigated.

Chapter 4 moves to single element trans rectal ultrasound (TRUS). The movement of the transducer during 3D acquisition is a spiral motion in the pull direction. A significant improvement in image quality when SAF is applied is shown for both simulations and phantoms. The two-step approach is most desirable here since the full volume is often of interest. The effects of having two interpolation steps is shown as well as the required steps needed to retaining a good image quality.

The appendix contains a reprint of the papers published during the course of the PhD or currently under review. The papers are contained in Appendix A to D. In addition a description of further work with a beamformation toolbox used at CFU is given in Appendix F, and a section with mathematical derivations in Appendix G.

OVERALL CHANGES TO DOCUMENT

Efficient aperture.... think it through a bit

Show acquisition movement form 2007/2008 conference slides. Can be included for better visualization

Overall, give better feel for how the data has been acquired. In papers but not readily available.

Read each chapter with a notion of what I want to tell, and is that accomplished. What is superfluous.

Use jakobs references to cfu-papers for better view of what has been done previously.

CHAPTER

TWO

Translated Linear Array

This chapter contains a presentation of the journal article

- Henrik Andresen, Svetoslav I. Nikolov and Jørgen A. Jensen, ”Precise Time-of-Flight Calculation for 3D Synthetic Aperture Focusing”, accepted for publishing in *IEEE Transactions on Ultrasonics, Ferroelectrics and Frequency Control*, 2009,

and the conference article

- Henrik Andresen, Svetoslav I. Nikolov and Jørgen A. Jensen, ”Precise Time-of-Flight Calculation for 3D Synthetic Aperture Focusing”, presented at *IEEE - Ultrasonics Symposium* in New York, New York, 2007, pp. 224-227,

which are found in full length in Appendix A and A.1, respectively. The journal paper is an extended and elaborated version of the conference paper, and, thus, primary focus will be put on the content of the journal paper. In addition a few results showing the performance of 3D SAF using linear arrays will be shown. These results are not unique to the method, but allows the reader to see the potential for improvement.

2.1 Purpose of the Study

As discussed in Section 1.2.3 the processing requirements for performing SAF in 3D become significantly higher compared to conventional beamforming. In an effort to reduce the computational cost the process has previously been performed in two steps [34]. In addition, no easy method of calculating the direct ToF for a focused linear array was available, which made conventional arrays undesirable for a direct SAF method because of the focusing lens. The two-step approach worked around this by using well known SAF methods in 2D and applied the focusing to each dimension separately.

This reduction in computational cost of the two-step approach comes at the cost of flexibility. The two-step approach has to cover the entire range of depth used in both steps with adequate sampling, regardless of whether many or few points are actually beamformed in the second step. This makes the processing requirement invariant to the resulting volume size, which is unfortunate if only a few points are actually used, and good because it is easy to estimate the highest processing load for real-time implementation. The direct approach only needs a single ToF and data-sample for each beamformed point, but each point requires to be beamformed for each emission, resulting in many more calculations per point.

A significant difference is also how a direct ToF and a two-step approach processes the information in the signal. In a direct ToF method only a single interpolation step is used. The two-step approach must contain the entire frequency content of the signal axially after the first step to supply adequate information for the second step. Because the second step requires an additional interpolation step, additional noise is introduced. It has been quantified how the second step is limited by the interpolation, and requires a more advanced interpolation when sampling close to the Nyquist criterium, or a denser sampling if linear interpolation is used. This is presented in more detail in Chapter 4.

This study has two main objectives. Developing a method for a direct ToF calculation and investigating the image and processing performance of the method. Additionally it was desirable to verify the improvement in elevation resolution when performing 3D focusing and the limitations in regard to sampling density. The chapter presents the results for a new ToF method that allows the beamforming to be done in a single step and scales directly with the number of imaging points. This allows a few points to be beamformed more efficiently and removes the need for moving large amounts of data between the first and second beamforming step.

2.2 Contributions

A direct method has to be able to calculate the ToF for a given point in three dimensions relative to the linear array. This will allow the beamforming to be done using only a single interpolation step and without moving the intermediate dataset to the second step. In addition it has to allow a vitual source (VS) in transmit to increase the emitted energy. The lateral, elevation, and axial direction will be denoted x, y, and z respectively. The VS used to increase emitted energy is denoted VS_{lat} and a VS used in elevation VS_{ele}.

The proposed method is visualized in a series of figures. Fig. 2.1 shows the initial setup, illustrating the transducer geometry and position of the desired beamformed point. The figure is split into three sub-figures, where Fig. 2.1(a) is the three-dimensional view, and Fig. 2.1(b) and 2.1(c) are projections in the $x-z$ and $y-z$ plane, respectively. The proposed method works by first projecting the point onto the $x-z$ plane as shown in Fig. 2.2, creating a virtual point denoted $\vec{r}_v$. The depth of the projected point is equal to the distance between $\vec{r}_p$ and a VS placed at the elevation focus of the transducer at the lateral position of the point. The equation for the depth is similar to (1.4) and given by

$$z_{\text{proj}} = \sqrt{r_{p,y}^2 + (r_{p,z} - \text{VS}_{\text{ele},z})^2} \cdot sign(r_{p,z} - \text{VS}_{\text{ele},z}) + \text{VS}_{\text{ele},z}, \tag{2.1}$$

where $r_{p,y}$ and $r_{p,z}$ is the elevation and depth position of $\vec{r}_p$ relative to the transducer, and $\text{VS}_{\text{ele},z}$ is the depth of the elevation VS. The projection is shown in 2.2 where the virtual point has the coordinates $(r_{p,x}, 0, z_{proj})$, and is used for the ToF calculation using 2D SA focusing. For this paper a de-focused VS is applied, but a small change to (1.4) will allow a focused VS to be allied both laterally and in elevation. The equation for the total ToF for a transmission to the m'th receive element is given by

$$t_{\text{ToF},m} = \frac{|\vec{r}_v - \text{VS}_{\text{lat}}| + |\vec{r}_v - \vec{r}_{rcv,m}|}{c}, \tag{2.2}$$

where VS_{lat} is the position of the transmit VS, $\vec{r}_{rcv,m}$ is the position of the m'th receiving element, and c is the speed of sound. The path is shown by the solid line in Fig. 2.3. The ToF

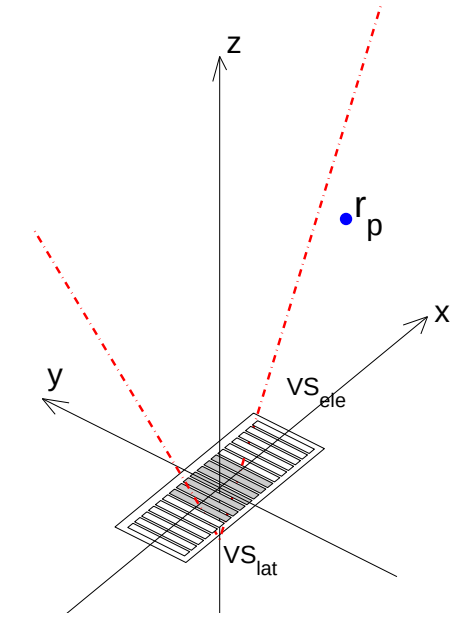

(a) 3D Illustration of the ToF calculation

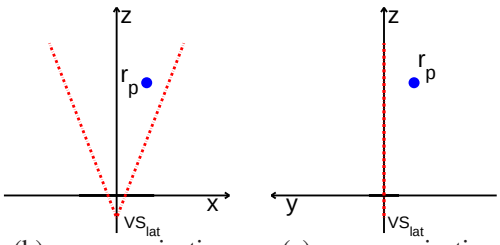

(b) $x-z$ projection (c) $y-z$ projection

Figure 2.1: Initial setup for the ToF calculation. The elements in the array is shown with the active elements for a VS transmission shaded gray, the red dotted lines are the lateral VS acceptance angle, and the blue point is the desired beamformed point.

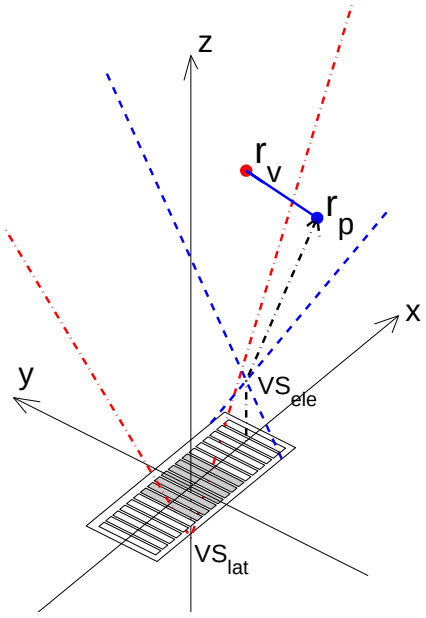

(a) 3D Illustration of the ToF calculation

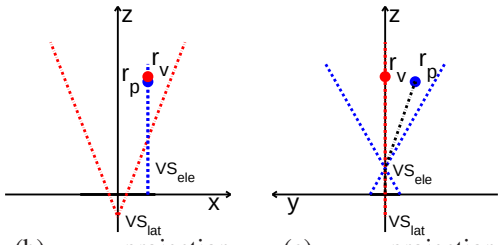

(b) $x-z$ projection (c) $y-z$ projection

Figure 2.2: Illustration of the point projection of the method. The point $\vec{r}_p$ is the desired beamformed point. The dashed lines represent the acceptance angle of a the elevation VS placed at the elevation focus. A virtual point $\vec{r}_v$ is created in the $x-z$ plane. The point is placed so the wavefront will reach both $\vec{r}_p$ and $\vec{r}_v$ at the same time.

given by (2.2) allows the data for each point to be calculated using only a single interpolation using the original RF-data.

The number of required samples as well as resulting resolution is highly dependent on the motion of the transducer. In this study the transducer was moved stepwise in the elevation direction where a full 2D image sequence was performed at each elevation position as shown in Fig. 2.4. This allows the generation of a conventional 2D image using SAF at each elevation position. The total signal amplitude for a single point is given by summing the received signals at the time instances calculated by (2.2), which yields

$$s(\vec{r}_p) = \sum_{j=1}^{J} \sum_{m=1}^{M} \sum_{n=1}^{N} a_{j,m,n} \cdot g_{j,m,n}(t_{ToF,m}), \tag{2.3}$$

where $a_{j,m,n}$ is the apodization, and $g_{j,m,n}$ is the signal for the m'th receive channel of the n'th emission at the j'th elevation position. M is the number of receive elements, N is the number of transmit VS's, and J is the number of elevation positions. Further details on acquisition and transducer parameters are found in Appendix A chapter IV of the paper.

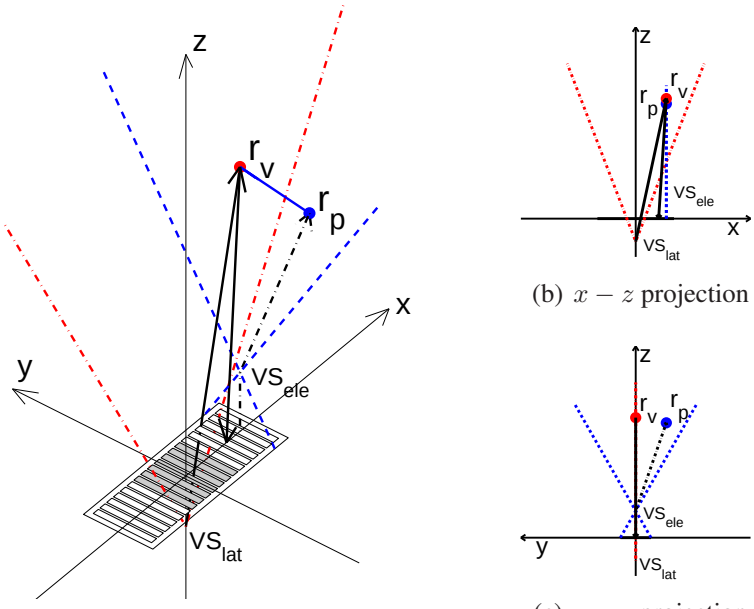

(a) 3D Illustration of the ToF calculation

(b) $x - z$ projection

(c) $y - z$ projection

Figure 2.3: The final step of the ToF calculation. To calculate the ToF for each receive channel, normal 2D SA focusing is used for the point $\vec{r}_v$. The solid line represents an example of a single transmit-receive path used for a receive channel.

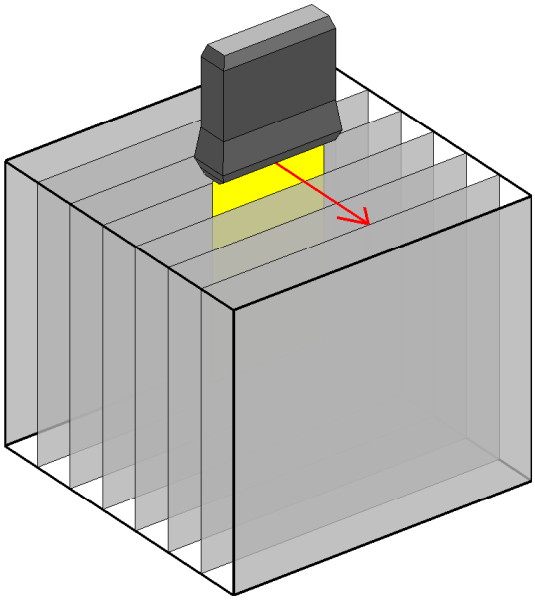

Figure 2.4: Illustration of acquisition with a linear array transducer. The full aperture is sampled at each image plane before moving to the next elevation position.

2.2.1 Processing

Considering the two beamforming approaches and the acquisition setup used, either approach can be set perform significantly better than the other depending on the desired resulting image. To give a fair view of different options, a comparison is made for a full volume rendering as well as for a single plane. A full volume is useful for post-scan evaluation, and three orthogonal

planes can be used to give real-time visualization.

Some assumptions are made in the comparison for the two beamforming methods. The resolution required for the first step in the two-step approach is assumed to follow the requirements set forth in [12]. Here the lateral and axial sampling density is defined according to (2.4) and (2.5). The calculation requirement for the two-step approach is also limited to the first beamforming step because the second step is significantly less demanding. The direct ToF method presented here is implemented in a custom beamformation toolbox. The implementation allows a fast removal of points outside the elevation acceptance angle, which significantly reduces the computational load. A similar discretization is not possible to implement for the first step in the two-step approach for either full volume or orthogonal plane view. For both methods a linear interpolation is used. The equations defining axial and lateral sampling is given by

$$\delta\theta \leq \sin^{-1}\left(\frac{\lambda}{\left(1+\frac{B_{\text{rel}}}{2}\right)D_{\text{eff}}}\right), \tag{2.4}$$

where λ is the wavelength, B_{rel} is the -6 dB relative bandwidth, and D_{eff} is the size of the effective aperture, which is the convolution of the transmit and receive aperture [38]. The number of axially beamformed points is required at a minimum of

$$N = \frac{4d(1+\frac{B_{\text{rel}}}{2})}{\lambda}, \tag{2.5}$$

where d is the sampling depth.

The chosen beamformed volume is equal to the volume covered by stacking the conventional 2D images. The volume is 140 mm deep, use a 90°sector view, and 27 mm in height. For the given transducer this will require 260 scan-lines per plane each with 2800 samples in each line based on (2.4) an (2.5). The number of points used in the two-step is simply given by

$$N_{\text{two-step}} = N_{\text{emis}} N_{\text{rcv}} N_{\text{axial}} N_{\text{lat}} N_{\text{ele}}, \tag{2.6}$$

where N_{emis} is the number of emissions per image plane, N_{rcv} is the number of receive elements, N_{axial} is the number of points per line, N_{lat} is the number of lines per image plane, and N_{ele} is the number of image planes. The required number of points for the direct ToF method has been counted by the method because the implementation uses a different number of points for each emission. The required points for the two-step ToF and the direct ToF method is shown in Table 2.1. The number of points clearly show the two-step beamforming uses an order of magnitude fewer points if a full volume is beamformed. By reducing the desired volume to only three planes the direct approach is able to perform this with fewer points because it scales better with the resulting volume. A significant gain can be won by choosing either method dependent on what is used, and even changing from one implementation to the other depending on the target volume.

Table 2.1: Required beamformed points for 3D SA focusing and the conventional 2-step beamforming.

Beamforming method	Full Volume	Single Plane
Two-step Beamforming	$0.90 \cdot 10^{12}$	$0.90 \cdot 10^{12}$
3D SA Beamforming	$1.03 \cdot 10^{13}$	$3.61 \cdot 10^{10}$

In addition to number of calculations, the two-step approach has to move the result from the first step to an intermediate storage. The transducer is stationary during the acquisition of each

imaging plane, which allows all emissions to be summed before moved to the second stage. If the transducer was moving this would not be possible without a degradation of the elevation focus. The number of values for the stationary case is equal to

$$B_{\text{stat}} = N_{\text{axial}} \cdot N_{\text{lat}} \cdot N_{\text{ele}} \tag{2.7}$$

The number for the moving case is equal to

$$B_{\text{mov}} = B_{\text{stat}} \cdot N_{\text{emis}} \tag{2.8}$$

The temporary storage required is equal to 219 MB for a semi-stationary acquisition, and 14 GB for a moving acquisition with the same number of emissions.

2.2.2 Imaging Results

Just as important as the performance characteristics of the method is its imaging performance. The results here are shown to verify the the methods ability to work on simulated and measured signals. In addition they show the performance of monostatic SAF in elevation using a moving array. Similar results have been shown in previous papers, but are included to show the benefits in both resolution and contrast when applying 3D SAF.

The evaluation of the image quality is performed by an analysis of the point spread function (PSF). The full-width at half-max (FWHM) is used as a measure of resolution and the main-lobe to side-lobe ratio (MLSL) is used to quantify contrast. The MLSL ratio is given by

$$\text{MLSL} = 10 \log_{10} \left(\frac{\sum_{n=n_1}^{n_2} s(n)^2}{\sum_{n=1}^{n_1-1} s(n)^2 + \sum_{n=n_2+1}^{N} s(n)^2} \right), \tag{2.9}$$

where $s(n)$ is the sampled PSF projected in the axial direction, and n_1 and n_2 is the index of the beginning and end of the main-lobe. The main-lobe is defined as the PSF above -40 dB. All PSF's are compared to the main-lobe of the elevation focused PSF with the smallest elevation step size. This will prevent a poorer focusing giving a better MLSL-ratio. The results presented here is a combination of simulations and measurements. Both simulations and measurements are performed using 64 emissions per imaging plane with a distance of 0.09 mm between each imaging plane equal to 0.41 λ. Additional description of the measurement setup is found in Appendix A.

The simulation uses at a set of point scatterers placed between 20 mm og 120 mm of depth. The FWHM is shown in Fig. 2.5. With no elevation focusing a linear increase of the FWHM is seen as a function of depth. By applying 3D focusing, the constant $F^{\#}$ allows for a near constant FWHM. The two-step focusing method shows results similar to the 3D focusing, but has a slightly larger FWHM at deeper lying scatterers.

!!!! If time allows, investigate side-lobes to confirm that sampling for the two-step was inadequate !!!!

By increasing the distance between each imaging plane it is possible to increase imaging speed as well as reduce computational cost. The results of changing the elevation step size are shown in Fig. 2.6 and 2.7. The FWHM is almost the same regardless of stepsize, since this is related to the width of the effective aperture. The MLSL shows a slight decrease in side-lobe level when the step size is changed from 0.5 to 2 λ. Above 2 λ the side-lobes become an increasing problem and the MLSL-ratio is decreased.

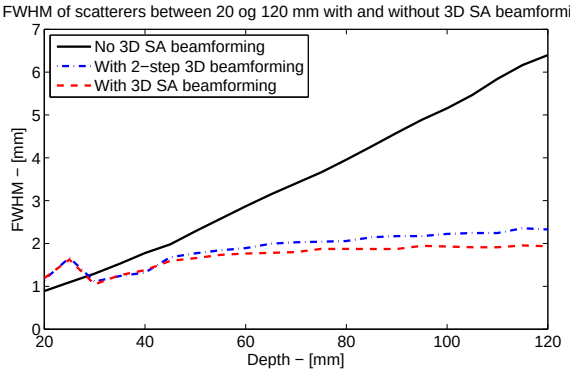

Figure 2.5: Elevation FWHM for scatterers between 20 and 120 mm, with no, 2-step, and with 3D focusing.

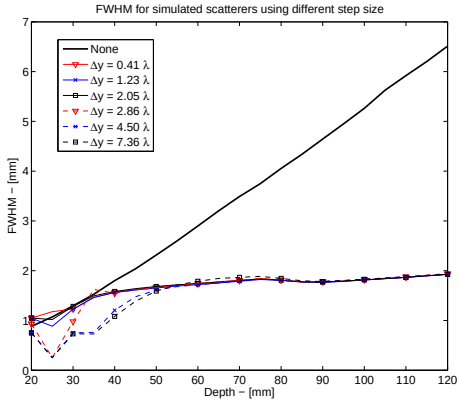

Figure 2.6: FWHM for simulated scatterers between 20 and 120 mm of depth. Each line represents a different step size in elevation.

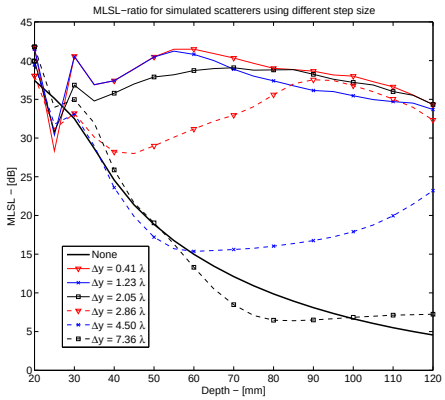

Figure 2.7: MLSL for simulated scatterers between 20 and 120 mm of depth. Each line represents a different step size in elevation.

To visualize how the step size develops with increased side-lobe level, a simulated point scatterer and a measured diamond scatterer at 65 mm of depth. Fig. 2.8 shows side-lobes below -60 dB for a stepping size of 0.41 λ, while for 2.05 λ they are below -50 dB. An increase of the elevation step size to 4.50 λ elevates the side-lobes to almost the same level as no 3D focusing. Result are similar for the measured PSF in Fig. 2.9, except all values are higher. The center part of the PSF is seen to be unchanged by the increase in stepping size as indicated by the constant FWHM.

The improvement in resolution and contrast will improve the image quality compared to simply stacking the image planes to form a 3D volume. The improvement is shown for a normal image plane and a C-scan when applied to data from a cyst phantom in Fig. 2.10 and 2.11, respectively. The image shows a single cyst in the Fig. 2.10 and two cysts in Fig. 2.11. The cysts are much clearer when 3D SAF is applied, which shows the potential in implementing 3D focusing.

2.3 Discussion

From an image quality perspective there exists high potential for improvements by implementing 3D SAF. This improvement does come at a cost, where several trade offs have to be considered. Regardless of the method used, it is possible to reduce computational costs by sampling

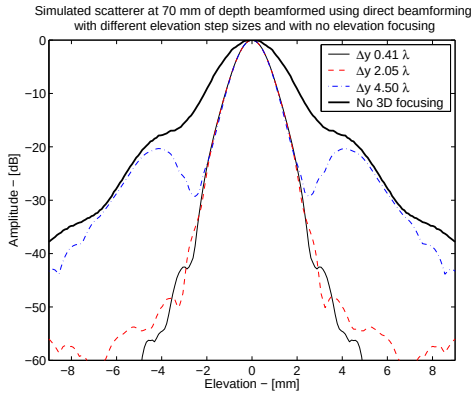

Figure 2.8: Projection of the PSF of a simulated scatterer at 65 mm of depth for different elevation step sizes.

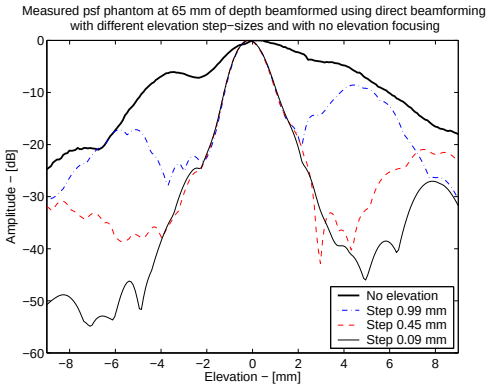

Figure 2.9: Projection of the PSF measured on a PSF phantom at 65 mm of depth for different elevation step sizes.

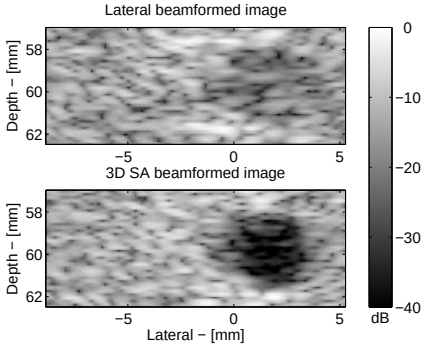

Figure 2.10: B-mode image of a cyst phantom with and without synthetic elevation focusing in the lateral-depth plane. The diameter of the cyst is 4 mm.

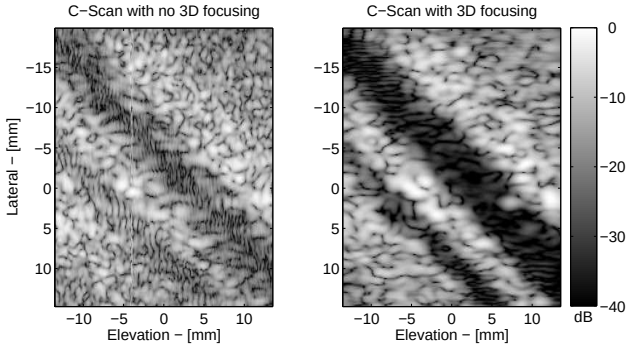

Figure 2.11: C-Scan of a cyst phantom with and without 3D focusing.

the elevation aperture more sparsely. It is shown that no significant side-lobes occur if the sampling distance was equal to 2λ for the current transducer. The sampling will be sensitive to the $F^{\#}$ of the transducer, where a low $F^{\#}$ requires a lower sampling distance and a high $F^{\#}$ allows a higher sampling distance.

The two methods were shown to perform differently depending on the desired outcome. If a full volume is desired the two-step method will initially be easiest to calculate. Several things have to be considered before either method is chosen or rejected. First is the beamforming implementation. The direct approach used a-priori rejection of points outside the acceptance angle. If this will increase implementation complexity to a much higher degree than implementing a 2D SAF without this rejection, it will possibly be too costly to implement a direct approach. A benefit of the direct approach is that it is less dependent on the signal, and only scales with the number of required points. The two-step approach scales with the frequency of the signal because the signal is beamformed twice. This will cause problems for the two-step approach if implemented for high center frequency or high bandwidth transducers like PMUT or CMUT transducers. In addition the storage required between the two beamforming steps can cause a significant increase in component cost as well as strain the bandwidth of the system.

Choosing either a direct or a two-step approach is seen to depend on both the transducer as well as the imaging needs of the system.

2.4 Conclusion

The results show that moving linear arrays have the ability to improve both resolution and contrast of ultrasound images. Using a direct ToF method has the potential for reducing costs compared to using a two-step approach if only a subset of a full-volume is desired.

A direct method will be most useful for a system, which has a high processing power but limited bandwidth. In addition, systems with high bandwidth using e.g. CMUT or PMUT arrays will benefit even further from the direct method since increases in signal-bandwidth also increases the required bandwidth for a system utilizing the two-step approach.

Results from the spiral paper in Chapter 4 also show the two-step method might be more costly than initial estimates due high side-lobes caused by interpolation errors. Further investigations in the possibility and costs of higher order interpolation have to be made.

The basic imaging properties for the method and for moving linear arrays show a potential for improving elevation focusing using existing arrays. For a three-plane visualization of a volume, the method allows a reduction of an order of magnitude in required beamformed points compared to previous methods. Also, the method only requires a single interpolation step and removes the requirement of an intermediate storage of beamformed data. This allows an implementation for systems, which do not depend on a full volume beamforming in real-time, using fewer resources.

CHAPTER

THREE

Rocking Convex Array

This chapter contains a presentation of the journal article

- Henrik Andresen, Svetoslav I. Nikolov, Mads M. Pedersen, Daniel Buckton and Jørgen A. Jensen, "Rocking Convex Array used for 3D Synthetic Aperture Focusing", submitted for publishing in *IEEE Transactions on Ultrasonics, Ferroelectrics and Frequency Control*, 2009,

and the conference article

- Henrik Andresen, Svetoslav I. Nikolov, Mads M. Pedersen, Daniel Buckton and Jørgen A. Jensen, "Rocking Convex Array used for 3D Synthetic Aperture Focusing", presented at *IEEE - Ultrasonics Symposium* in Beijing, China, 2008, pp. 970-973,

which are found in full length in Appendix B and B.1, respectively. The journal paper is an extended and elaborated version of the conference paper, and, thus, primary focus will be put on the content of the journal paper.

3.1 Purpose of the Study

Allowing real-time 3D imaging of tissue with a good elevation focus is desirable for several reason as described in the Introduction of this thesis. The linear array used in Chapter 2 was moved using precision motors in a fixed setup. This is generally a poor choise for in-vivo measurements since human anatomy and the transducer to tissue interface rarely allows linear motion in exact back-forth motion with good results to either image or patient. To allow the collection of in-vivo data a convex rocking array was used, which allows a large scan-angle in elevation as well as a good imaging of the abdominal region. The array moves continuously and can acquire several volumes per second.

In Chapter 2.2.1 it was shown that performing the data-processing using a two-step beamforming approach requires a large temporary storage. The temporary storage available at CFU is physical hard-drives, which have poor transfer rates compared to memory. Since processing is comparably cheaper, this makes the direct 3D SAF method described in Chapter 2.2 desirable. This method is slightly changed to encompass the more complex transducer geometry and moving acquisition.

Because the transducer array used has been developed with conventional imaging in mind, the elevation $F^{\#}$ of the array is high in order to control the width of the beam. This creates a

very narrow acceptance angle in the elevation plane, see (1.3). Using SAF for a moving array raises several issues because of the elevation VS approach. The following issues are either tried solved or investigated in the paper:

- For a transducer moving continually in elevation, only a few to a single emission will be within the acceptance angle near the elevation focus.
- The high $F^{\#}$ makes the point spread function (PSF) very broad at the focal point. A simple VS, which converges to a single point, is a poor model for the waveform.

Using conventional apertures with a narrow beam reduce the potential of SAF. Redesigning the transducer with a different elevation focus would allow more lines to be combined, giving a larger effective aperture. Simulations of different aperture designs will be investigated, assuming the same general design and motion as the original transducer.

3.2 Contribution

The direct SAF method described in Chapter 2 was modified to work with a convex rocking array. Because of the curvature and rocking motion, the direction of the virtual source in both elevation and transmit is rotated. To ease a description of the ToF, the desired point is rotated to keep a simple geometry of the VS propagation. The rotation is set so the VS emits along the new z-axis and the acceptance angle of the VS is placed symmetrically around the z-axis. The rotation is first done to counter the elevation rocking motion and second the move the transmit VS to the center. The two equations are given by

$$\hat{r}_p = (\vec{r}_p - \vec{v}_{\text{ele,origo}}) \cdot \mathbf{M}(\phi) + \vec{v}_{\text{ele,origo}} \tag{3.1}$$

$$\tilde{r}_p = (\hat{r}_p - \vec{v}_{\text{lat,origo}}) \cdot \mathbf{M}(\theta) + \vec{v}_{\text{lat,origo}}, \tag{3.2}$$

where $\vec{r}_p$ is the point of interest, $\tilde{r}_p$ is the final rotated point, $\vec{v}_{\text{ele,origo}}$ is the point of rotation for the elevation rocking motion, and $\mathbf{M}(\phi)$ is the rotation matrix around the x-axis, $\vec{v}_{\text{lat,origo}}$ is the point of origin for the convex array curvature, and $\mathbf{M}(\theta)$ is the rotation matrix along the rotated y-axis. The two matrices are given by

$$\mathbf{M}(\phi) = \begin{bmatrix} 1 & 0 & 0 \\ 0 & \cos(\phi) & \sin(\phi) \\ 0 & -\sin(\phi) & \cos(\phi) \end{bmatrix}$$

$$\mathbf{M}(\theta) = \begin{bmatrix} \cos(\theta) & 0 & -\sin(\theta) \\ 0 & 1 & 0 \\ \sin(\theta) & 0 & \cos(\theta) \end{bmatrix}$$

The entire ToF path is shown in Fig. 3.1, using the rotated coordinate system, where the point $\tilde{r}_p$ is the desired beamformed point, the dotted lines in the $\tilde{x}$-$\tilde{z}$ plane show the acceptance angle for the transmit VS and the dashed lines show the acceptance angle for the VS placed at the elevation focus. The lateral VS is denoted VS_{lat} and the elevation VS is denoted VS_{ele}.

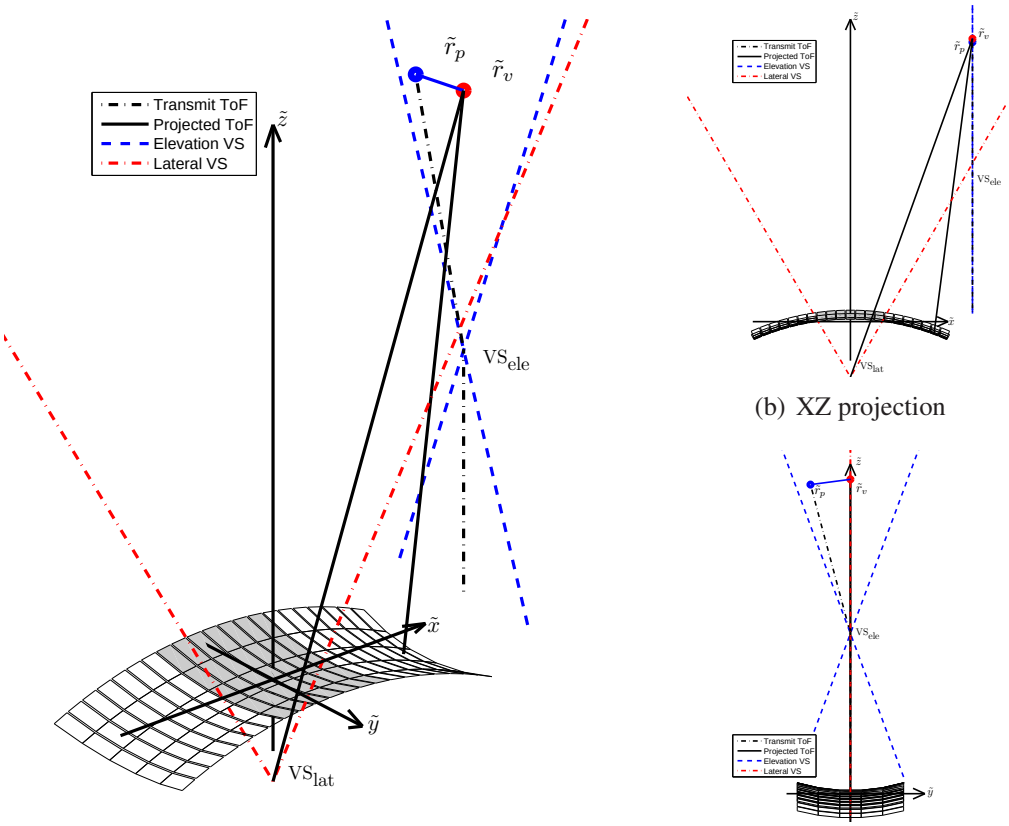

(a) 3D Illustration of the ToF calculation

(b) XZ projection

(c) YZ projection

Figure 3.1: Illustration of the ToF calculation. Red dotted lines are transmit VS acceptance angle, blue dashed lines are elevation focus acceptance angle, the dotted black line is transmit ToF for the beamformed point, and solid black line is the total ToF for the projectet point. The blue point $\tilde{r}_p$ is the desired beamformed point, and the red point $\tilde{r}_v$ is the virtual projected point. Figures (b) and (c) are projections in the XZ and YZ plane respectively.

The equations used for calculating the ToF for the rotated coordinate system are identical to (2.2) except for the introduction of the rotated coordinate system. The path is shown by the solid black line in Fig. 3.1(a). The signal amplitude for a single point is given by summing the received signals at the time instances calculated by (2.2), which yields

$$s(\vec{r}_p) = \sum_{m=1}^{M} \sum_{n=1}^{N} a_{m,n} \cdot g_{m,n}(t_{ToF,m}), \tag{3.3}$$

where $a_{m,n}$ is the apodization and $g_{m,n}$ is the signal for the m'th receive channel of the n'th emission. M is the number of receive elements and N is the number of transmit VS's. The equation only contains an emission index, since multiple emissions at the same elevation position is impossible due to the continuous motion.

3.2.1 Wide Plane-Wave Virtual Source

Near the elevation focus point only few emissions will be within the acceptance angle of the elevation VS, which limits the number of emissions usable for the lateral focusing. Laterally the focusing will be very sparse with only a few emissions, resulting in a degradation of the image quality.

To increase the number of emissions laterally the restriction from the acceptance angle has to be reduced to allow more emissions to contribute. By increasing the acceptance width to allow a full lateral aperture to be sampled at the narrowest point will solve the problem. Another arises because of the VS model used in the elevation plane. The conventional VS does not give a good description of the wave propagation outside the acceptance angle, giving rise to artifacts if used directly. Instead of isotropic propagation, a plane wave description is used at the elevation position and a combination of the two at a limited distance near the elevation VS. The plane wave ToF is calculated using conventional 2D SAF disregarding the elevation focus, as this will be invariant to elevation position. The weighting between each ToF method is calculated with a Hanning weighting, giving a combined ToF of

$$t_{\text{comb},m} = w \cdot t_{3D,m} + (1 - w) t_{2D,t}, \tag{3.4}$$

where $t_{3D,m}$ is the 3D direct ToF of the m^{th} emission, $t_{2D,m}$ is the conventional 2D SAF ToF, and w is the weighting function and given by

$$w = \begin{cases} \frac{1}{2}\left(1 + \cos\left(\pi \frac{\tilde{z} - z_{\text{ele}}}{z_{\max}}\right)\right), & |\tilde{z} - z_{\text{ele}}| \leq z_{\max} \\ 1, & |\tilde{z} - z_{\text{ele}}| > z_{\max} \end{cases} \tag{3.5}$$

Fig. 3.2 and 3.3 show the delayed and apodized RF-lines before summation marked with the expanded acceptance angle. The scatterers above and below the virtual source have been correctly delayed. At the focal point Fig. 3.2 shows a circular propagation, which is what the VS-model is assuming. The sum of these lines will be very different from what is desired, and give a much lower value than if the signal is summed in phase. Fig. 3.3 shows the result from the combined ToF equation, which allows several emissions to contribute in the lateral plane without creating destructive interference.

An illustration of the effect on the lateral PSF is shown in 3.4. The old VS description with a narrow acceptance angle results in higher side-lobes, reduced resolution and an asymmetrical peak. This is completely avoided by the combined VS description.

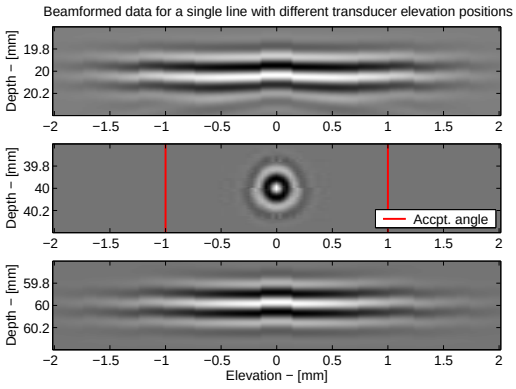

Figure 3.2: Delayed pre-summed data for a single scatterer measured with a translation of the transducer in the elevation direction. The data are beamformed using a simple isotropic VS model.

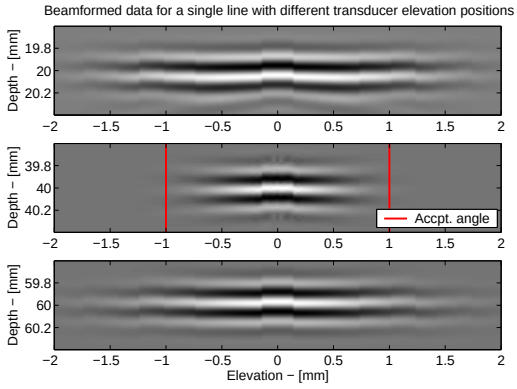

Figure 3.3: Delayed pre-summed data for a single scatterer measured with a translation of the transducer in the elevation direction. The data are beamformed using a combination of plane-wave and simple isotropic VS model. The plane-wave allows more lines near the focal point to be used.

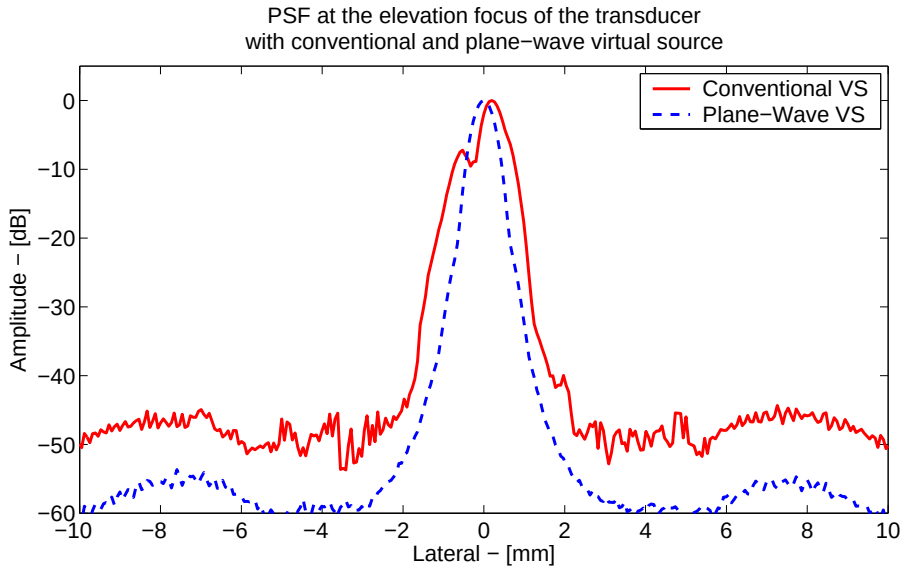

Figure 3.4: Two PSFs beamformed with a conventional isotropic and a new plane-wave virtual source.

3.2.2 Phantom and In-Vivo Measurements

The translated linear array presenten in Chapter 2 showed significant improvements when applying 3D SAF compared to simply stacked 2D images. Evaluating the performance of the rocking array is done using a wire phantom and several in-vivo measurements. The wire phantom is used to give an indication of the performance of the 3D SAF method used in combination with the transducer, to allow a better evaluation of how well the in-vivo measurements perform. The rirw-phantom is further evaluated with simulated scatterers to verify the results. For comparison, conventional 2D SAF was used to create a series of images, which were stacked to generate a 3D volume. Each 2D plane was beamformed using the closest emissions to the

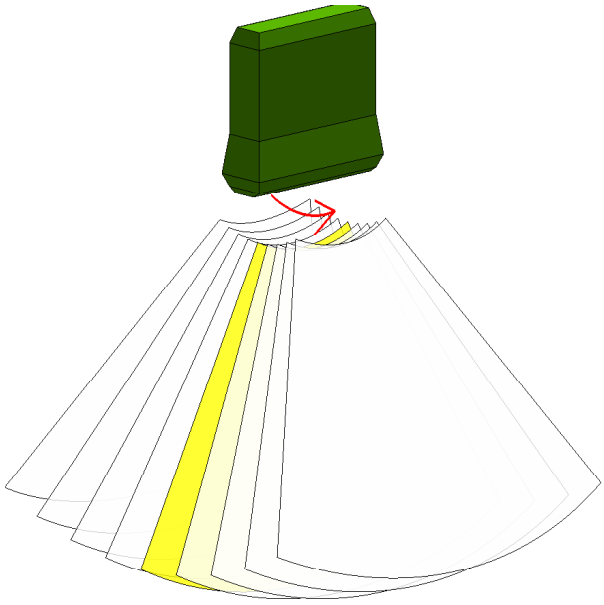

Figure 3.5: Visualization of the acquisition motion of the transducer as well as plane orientation.

plane angle, and beamformed using conventional 2D SAF ignoring the rocking motion. An illustration of motion and plane orientation is shown in Fig. 3.5. Each plane was generated using 80 emissions across the aperture and using 64 elements in receive. The results from the wire-phantom was in addition compared with simulations to validate the results. The transducer is basically a convex array submerged in a liquid behind a rubber screen, serving as the interface to the patient. An image of the transducer is found in Appendix H.1.

In Fig. 3.6 is an overlay of the elevation FWHM calculated from a volume created by 2D stacked slices compared with the results created using 3D SAF. The simulations and measurements show good agreement in both relative and absolute improvement. The improvement is between 20% and 40% indicating a noticeable reduction in scatterer size should be visible in in-vivo measurements.

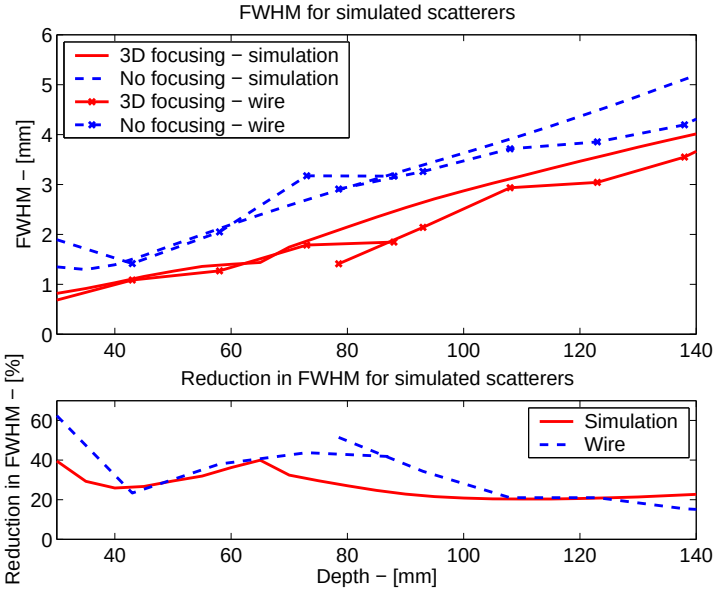

Figure 3.6: FWHM for simulated scatterers and measured wires with and without 3D SA focusing. The gain is calculated for both the measured and simulated scatterers.

Having shown the method and transducer was viable for 3D SAF focusing, a series of in-vivo measurements were performed on healthy male volunteers. Four images have been selected as exapmples of the method, which are shown in Fig. 3.7 paired with images created by stacked 2D slices. The target area was the right lumbar region allowing a view of the liver. Fig. 3.7(a) and 3.7(b) show a vein in the middle right part, but of most interest is the speckle in the liver. The images clearly show a reduction in the elevation direction, confirming the simulation and wire phantom measurements. Fig 3.7(c) and 3.7(d) show a C-scan of two veins, one going through the imaging plane to the left and one parallel to the plane at the lower right. The speckle is reduced in the elevation direction and the edge definition is better for the veins. A downside of the image is the artifacts near the edges, which blur the image. Figures 3.7(e) and 3.7(f) are a conventional B-scan, except placed in the elevation plane instead of the conventional lateral plane. They also an improvement in the elevation resolution and a better edge-definition of some of the blood vessels in the image.

The artifacts introduced by the 3D SAF, which are visible in spots around the images, are very clear in Fig. 3.7(g) and 3.7(h). The origin of these artifacts is not fully understood, but can

originate from both uncertainty of the rocking motion of the transducer, effects caused by the shell covering the rocking array, or another unfortunate side-effect from the transducer design.

3.2.3 Simulations and Transducer Design

As mentioned in Section 1.2.1, the basic limitation of SAF using virtual sources is the inability to increase the resolution beyond the $F^{\#}$ of the VS, which was used to acquire the data. Conventional ultrasound transducers are designed with a higher $F^{\#}$ to create a narrow beam in elevation, which limits the number of emissions that can be combined. Reducing the $F^{\#}$ can be achieved by having a shallower focus depth or increasing the height of the transducer elements. A change in elevation focus is largely dependent of the focusing lens added to the transducer, and can be done without changing other parts of the transducer like e.g. housing and wiring. Fig. 3.8 shows the acceptance angle for different elevation focus depths. Having a lower $F^{\#}$, coveres a much larger area with each emission. This larger acceptance angle spreads the energy over a larger volume, making it important to compare the gain in resolution to the effect on SNR. An estimate of the gain in SNR is derived in Appendix G.1 and given by

$$\text{SNR}_{\text{gain}} = \frac{p_{\text{sp}}^2}{p_{\text{sp},F^{\#}=5.5}^2 \sum_{n=1}^{N} a_n^2}, \tag{3.6}$$

where p_{sp} is the amplitude at the spatial peak of the investigated scatterer, $p_{\text{sp},F^{\#}=5.5}$ is the amplitude of the scatterer using an $F^{\#}$ of 5.5, and a_n is the apodization value from (3.3). This estimate compares the increase in the peak energy of a PSF with the added noise energy, calculated by the sum of variances.

The full width at half max (FWHM) is calculated for a set of simulated scatterers and for measurements performed on a wire phantom. To validate that the increase in resolution is not attained at the cost of higher side-lobes, the main-lobe to side-lobe ratio (MLSL) is calculated for the simulated scatterers. The main-lobe width used to calculate the MLSL is defined at -20 dB for the PSF created with 3D SA focusing. The MLSL ratio is calculated by

$$\text{MLSL} = \frac{\sum_{n=n_1}^{n_2} s(n)^2}{\sum_{n=1}^{n_1-1} s(n)^2 + \sum_{n=n_2+1}^{N} s(n)^2}, \tag{3.7}$$

where $s(n)$ is the sampled PSF projected in the lateral direction, and n_1 and n_2 is the index of the beginning and end of the main-lobe. Using simulated scatterers between 20 mm and 120 mm of depth with an $F^{\#}$ from 1.0 to 5.5, the FWHM and MLSL-ratio is shown in Fig. 3.11 and 3.12. The FWHM shows a large gain in resolution is possible if using a lower $F^{\#}$, although very low values might be impractical. The MLSL values also show that the improvement in resolution are not causing large side-lobes, which is seen from the largely constant values, as large side-lobes would show as a significant reduction in MLSL.

An investigation using a single scatterer at 70 mm of depth is shown in Fig. 3.9. Here it can be seen that a reduction in $F^{\#}$ improves the resolution but also has significant side-lobes. The side-lobes are caused by edge-waves generated by the transducer and enhanced by the elevation focusing. To suppress these side-lobes a hanning apodization along the elevation direction of the elements is used. Element apodization is not common but has been investigated in [39, 40, 41]. The effect of this apodization is seen in Fig. 3.10 where the side-lobes are attenuated. The main-lobe is also seen to widen, which is caused by the weighting. All other

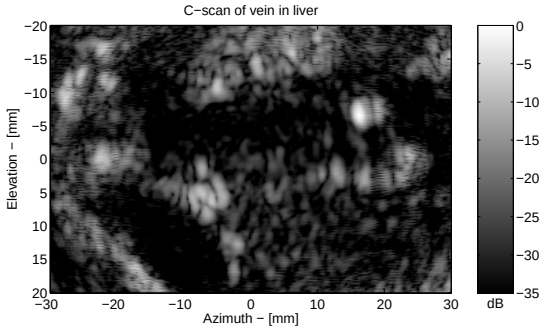

(a) C-scan of liver vein using 3D SAF

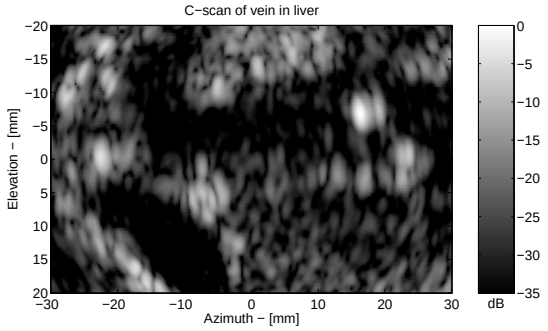

(b) C-scan of liver vein with no elevation focusing

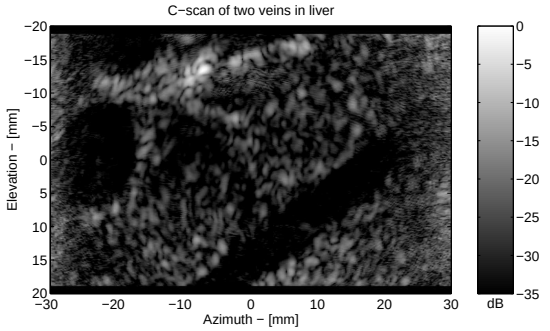

(c) C-scan of two liver veins using 3D SAF

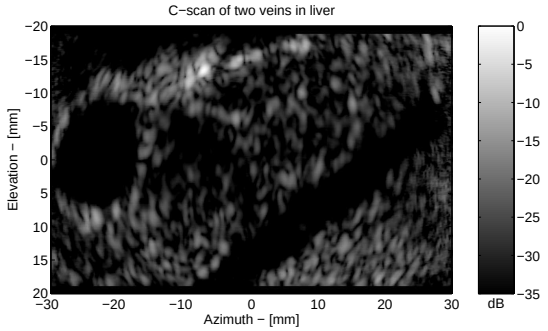

(d) C-scan of two liver veins with no elevation focusing

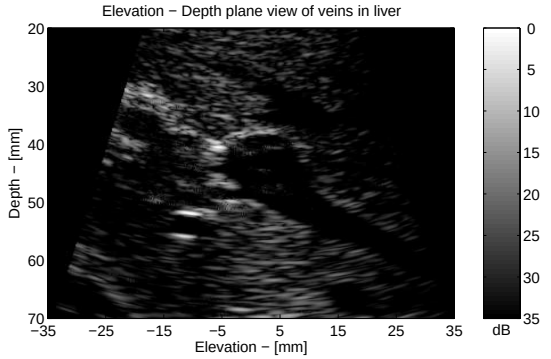

(e) Elevation plane of liver using 3D SAF

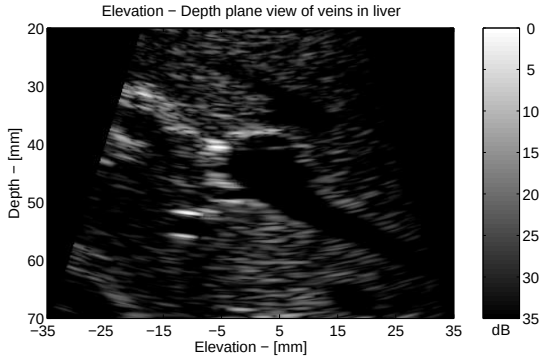

(f) Elevation plane of liver with no elevation focusing

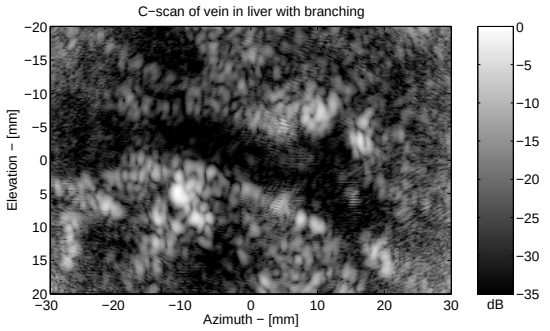

(g) C-scan of liver vein branch using 3D SAF

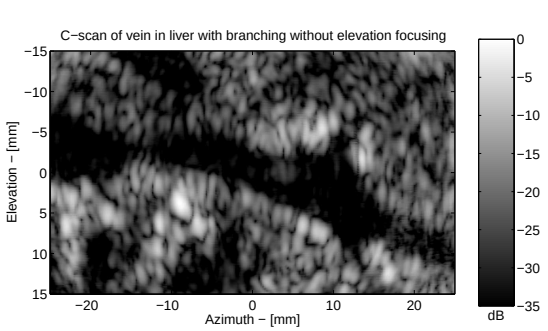

(h) C-scan of liver vein branch with no elevation focusing

Figure 3.7: In-vivo measurements showing three C-scans and an elevation B-scan of three healthy male volunteers

results will be presented using this apodization, which reduces the potential resolution but retains a good overall quality of the PSF.

In Fig. 3.8 it was shown that the lower $F^{\#}$ spreads the energy over a larger area. Even though more emission can be combined, each emission introduces an additional amount of electronic noise in total. The effect on the SNR is shown in Fig. 3.13. Two trends are worth noting the this figure. The increase around the focal point of the original transducer and the reduction in SNR elsewhere, especially for low $F^{\#}$s. Since the original $F^{\#}$ of 5.5 creates a broad beam at the focus, a lot of energy will be left out, even when using a wide VS as described in Section 3.2.1. Moving the focal point up allows this energy to be utilized. A similar effect is seen in reverse by a drop in SNR at the focal point of the other $F^{\#}$'s focus depth. The drop in SNR overall is caused by the increase in combined emissions, and from that the introduction of additional noise, without a significant increase in signal energy.

3.3 Discussion

Moving from a quasi-stationary acquisition to continuous motion was shown to be possible but required several changes to the current 3D SAF method. The method showed improvements in resolution and edge definition in in-vivo and phantom measurements, but also introduced artifacts on the in-vivo images. The artifacts shown in the in-vivo measurements were not shown in simulations or simple measurements. Having a more accurate model of the screen covering the transducer may allow a better description of the wavefront and improve image quality even further.

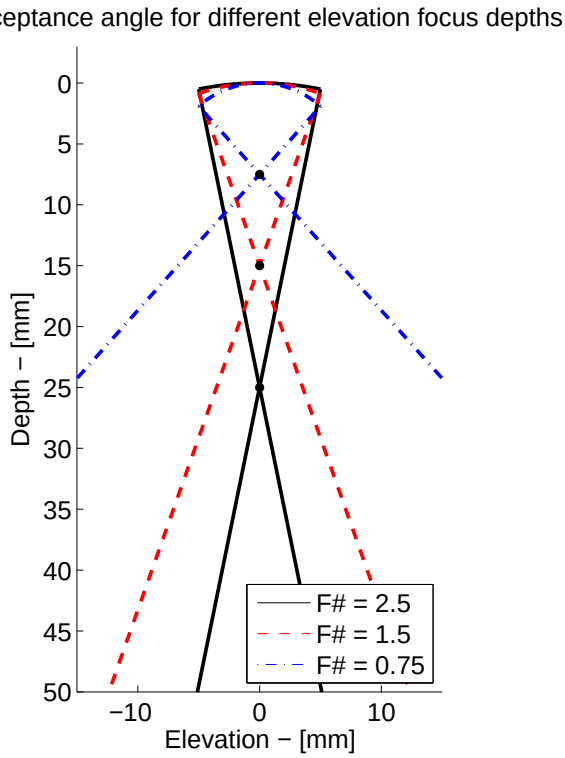

Figure 3.8: Visualization of the acceptance angle for the elevation virtual source for different elevation focus depths.

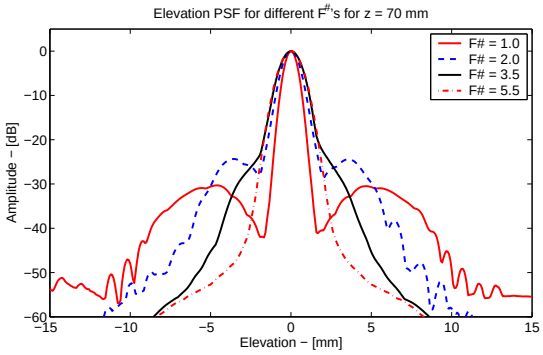

Figure 3.9: Elevation PSF for a scatterer placed at 70 mm of depth for different $F^{\#}$'s without transducer element apodization .

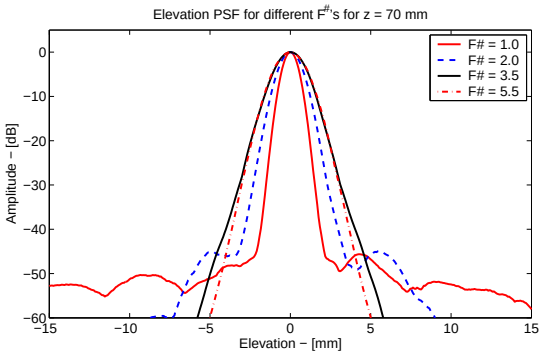

Figure 3.10: Elevation PSF for a scatterer placed at 70 mm of depth for different $F^{\#}$'s with a hanning transducer element apodization .

Changing the transducer design showed a potential for improving the current resolution in 3D images with relatively cheap technology. Unfortunately they are a trade-off between several desired properties. If the $F^{\#}$ is reduced to allow a better focusing, a single emission will contribute to a large part of the volume. This will also make the method more sensitive to shadowing from bones or poor interface between transducer or patient. If no signal returns a larger part of the volume will only receive the electronic noise from the transducer, and the overall SNR will drop because it depends on the correct summation of more emissions. Another aspect is the more well defined elevation focus. If an $F^{\#}$ of 2 is used in elevation, the width used for a wide plane wave VS will be much narrower, reducing the number of possible emissions making up the lateral image. So a trade-off between having a good lateral resolution at the focal point and a good elevation resolution has to be made.

A transducer design beneficial for 3D SAF might be a defocusing lens in elevation, which will altogether remove the need for a plane-wave VS. It will also allow a more powerful emission since the entire wave will be defocused reducing the intensity, leaving more room before FDA limits are reached [42]. This will make it more susceptible to shadowing as mentioned before, so this limits the areas where the transducer can be applied. In addition, making it effective for 3D SAF will make it just as poor for conventional 2D imaging, so either the transducer will not

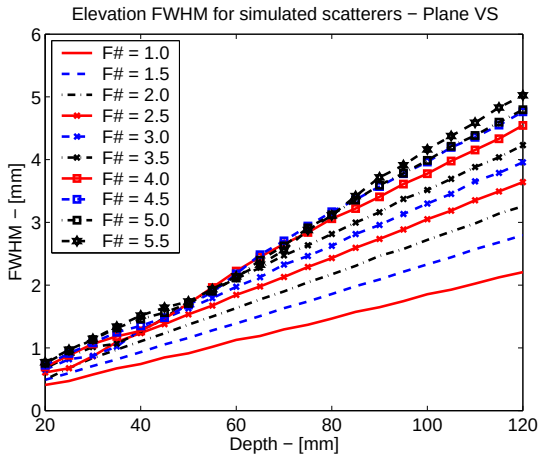

Figure 3.11: Elevation FWHM for scatterers placed between 20 and 120 mm of depth using different elevation focus.

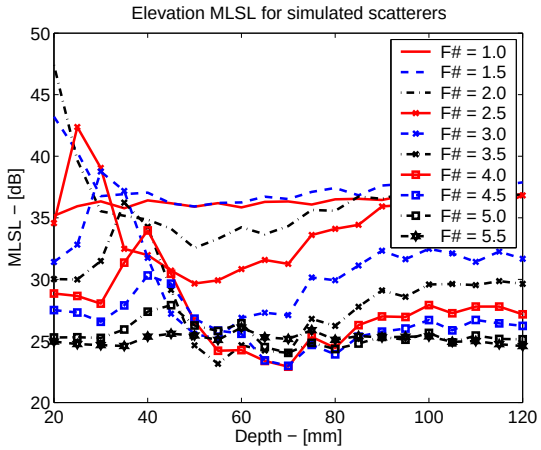

Figure 3.12: Elevation MLSL for scatterers placed between 20 and 120 mm of depth using different elevation focus.

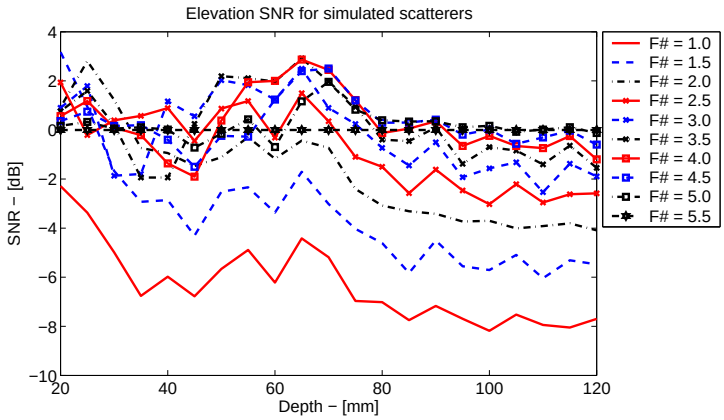

Figure 3.13: Elevation SNR for scatterers placed between 20 and 120 mm of depth using different elevation focus.

be useful in 2D imaging at all, or it has to be made as a 1.5D array with a simple switching to change the fixed $F^{\#}$ depending on the acquisition mode.

The application of 3D SAF to rocking arrays has clear potential for giving a better image, allowing a better diagnosis of patients. A drawback is the trade-offs, which will make a given transducer design specific in use to e.g. liver measurements or fetal facial imaging, and not an overall transducer with a very wide range of uses.

3.4 Conclusion

The method for 3D SAF has been successfully implemented for a rocking convex array. The method is able to improve the elevation resolution for a measured wire-phantom, and show a good agreement between measurements and simulations.

Overall, the method has the potential of improving both resolution and contrast significantly by a better transducer design. A transducer designed for better utilization of 3D SAF will have an $F^{\#}$ of around 2-3 as well as an apodization in elevation to reduce edge-waves. It is possible to choose a design with improved resolution, contrast and SNR around 60 mm of depth, which is the depth of interest for the current transducer, but at a cost of a slight reduction in penetration. A trade-off between SNR and image quality has to be made if the $F^{\#}$ is reduced even further. A drawback of making this change in transducer geometry is that the transducer will have very poor imaging qualities using conventional 2D imaging for orientation, limiting the transducer to 3D imaging. In addition it will be more sensitive to a poor patient transducer interface

Several 3D in-vivo volumes were acquired from healthy volunteers and compared to a conventional 2D SAF approach. The results for the current transducer show a mix of improvement and artifacts. The artifacts and ability to improve resolution could be improved with a better transducer design and understanding of the propagating wave.

CHAPTER

FOUR

Spiral Motion Synthetic Aperture Focusing

This chapter contains a presentation of the journal article

- Henrik Andresen, Svetoslav Ivanov Nikolov and Jørgen A. Jensen, ”Synthetic aperture focusing for a single element transducer undergoing spiral motion”, submitted for publishing in *IEEE Transactions on Ultrasonics, Ferroelectrics and Frequency Control*, 2009,

which is found in full length in Appendix C.

4.1 Objective of the Paper

Single element transducers are used if size or cost need to be limited. The element can be small enough to be fitted within a catheter for e.g. endo-cardio scans and only require a single DAC, making the receive system very cheap. Using single element transducers is limited by two factors, they need mechanical motion to create an image and their useful range of depth is small because of the fixed focus. Applying SAF to a single element transducer has been done often as mentioned in the introduction. A rotating transducer is not used often, and for a system with slightly different parameters, only an increase in SNR was found [43]. The transducer used in this paper is designed for analyzing the rectal wall for cancer investigation, but the results can be applied to any rotating transducer geometry. A better resolution and imaging quality will allow better results in both cancer treatment and detection [2, 44].

The transducer rotates and translates simultaneously, which creates a spiral motion. This allows SAF to be applied in 3D in two ways. The direct method is treating the elevation focus as a virtual source and using the direct distance in three dimensions. An alternative is focusing using two steps as has been done previously [13, 34]. A focus in the paper is the performance of the two methods as well as processing requirements.

4.2 Contribution

Conventional imaging with the rotating single element transducer creates an image plane per revolution through scan-conversion and stacks the imaging planes to create a 3D volume. These

images have a good image quality at the focal point of the transducer and a quick reduction above and below the focus point. The motion of the transducer is shown in Fig. 4.1. The application of SAF is done using both a direct approach and a two-step approach. The two-step approach focuses first in azimuth and second in elevation. This allows an easier implementation of this approach in a real scanner since the data will be acquired one plane at a time.

The circular element has a virtual source (VS) with a circular symmetric time-of-fligt (ToF) and acceptance volume. The ToF is calculated by using (1.6) from Section 1.2.1 for the two-step approach, and similarly for the direct approach the ToF is given by

$$T(\vec{r}_p) = \frac{2}{c}\left(|\vec{r}_p - \vec{\mathrm{VS}}_{\mathrm{foc}}| \cdot \mathrm{sign}(r_{p,z} - z_{VS}) + z_{VS}\right), \tag{4.1}$$

where c is the speed of sound, $\vec{r_p}$ is the point of interest, $\vec{\mathrm{VS}}_{\mathrm{foc}}$ is the position of the virtual source, $r_{p,z}$ is the depth of the point of interest, and z_{VS} is the depth of the virtual source. It is

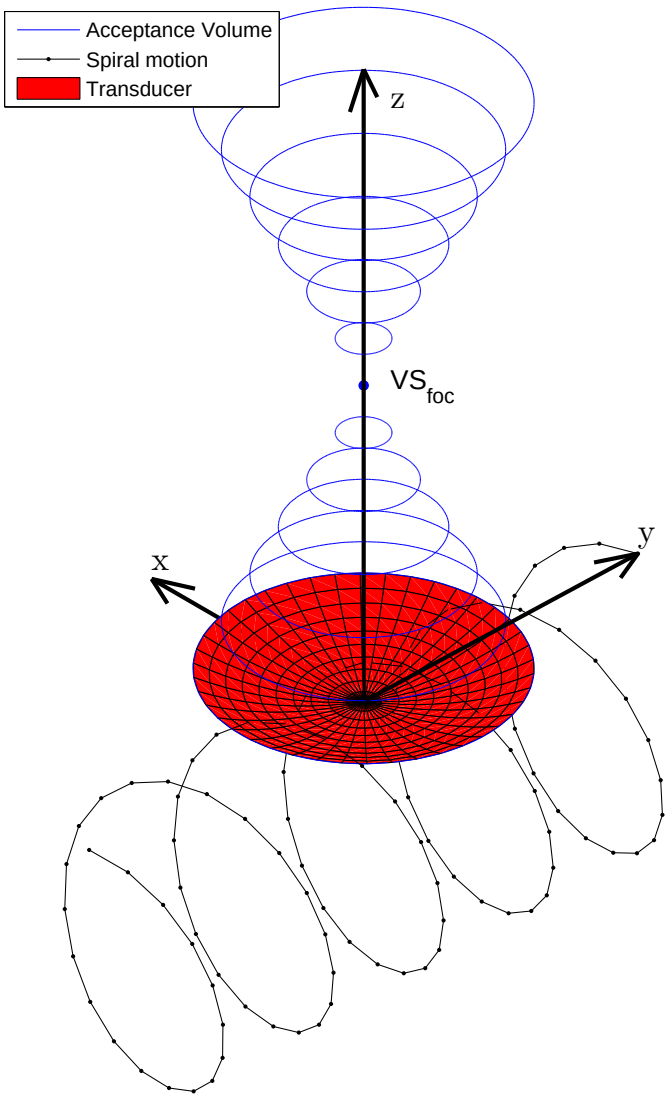

Figure 4.1: Visualization of the motion and virtual source for the transducer. The blue rings show the limits of the acceptance volume, the black dotted line shows the motion of the element and the large surface represents the actual transducer.

assumed the transducer is positioned at $\vec{r} = (0, 0, 0)$ and the direction of propagation is along the z-axis for easier notation.

The two approaches should ideally give the same resulting ToF, which allows the same imaging quality. The equation used are exactly the same except the points in the two-step approach are only assumed to have two dimensions. The beamforming of a given point using the direct approach is calculated by

$$p(\vec{r}) = \sum_{n=1}^{N} a_n s_n(T_n(\vec{r})), \tag{4.2}$$

where N is the total number of contributing emissions, a_n is the apodization for the n'th emission, $s_n(t)$ is the received signal from the n'th emission at time t, and $T_n(\vec{r})$ is the ToF. As the transducer is both moving and rotating, the coordinate system is rotated around the transducer to allow the ToF calculations to be made by (4.1).

Combining several emissions in phase will allow an increase in signal-to-noise ratio (SNR). Because the motion of the transducer makes several identical imaging sequences very difficult, the increase in SNR will be estimated by

$$\text{SNR}_{\text{gain}} = \frac{p_{\text{sp,saf}}^2}{p_{\text{sp,uf}}^2 \sum_{n=1}^{N} a_n^2}, \tag{4.3}$$

where $p_{\text{sp,saf}}$ is the amplitude at the spatial peak of the investigated scatterer, using a SAF beamforming approach, $p_{\text{sp,uf}}$ is the amplitude of the unfocused approach, and a_n is the apodization value from (4.2). The derivation is given in Appendix G.1. To evaluate the contrast of the cyst phantom a contrast-to-noise ratio (CNR) is calculated from [45] and given by

$$\text{CNR} = \frac{|\mu_s - \mu_c|}{\sqrt{0.5 \cdot (\sigma_s^2 + \sigma_c^2)}}, \tag{4.4}$$

where μ_s and μ_c are the mean-value of the speckle and cyst area, respectively, and σ_s^2 and σ_c^2 are the variance of the speckle and cyst area.

4.2.1 Simulation

To validate the performance of the system a series of point scatterers was simulated. The scatterers were placed between 15 mm and 100 mm of depth with the motion of the array identical to that of the physical array investigated. The array and scan-sequence is described in further detail in Appendix C. To establish how well SAF would perform for the given geometry, a simple test with only rotation or translation was made. Fig. 4.2 shows the improvement in FWHM for the 2D SAF. It shows that SAF is able to hold a constant $F^{\#}$ in elevation for the desired depth, but is limited by the rotational axis in azimuth. A significant improvement is seen in both cases. A comparison of the resolution achieved by 2D SAF with the potential of 3D SAF is shown in Fig. 4.3 and 4.4. Here is a slight increase in azimuth resolution and the same resolution in elevation. The two methods are also seen to perform almost identically.

The resolution of both 3D SAF methods is almost identical and near that obtained for a 2D SAF in either dimension. Of equal importance to image quality is the side-lobe level of a PSF, which gives an indication of the possible contrast of an imaging method. In azimuth the two-step and direct SAF method yields almost identical PSFs, but in elevation a large difference in

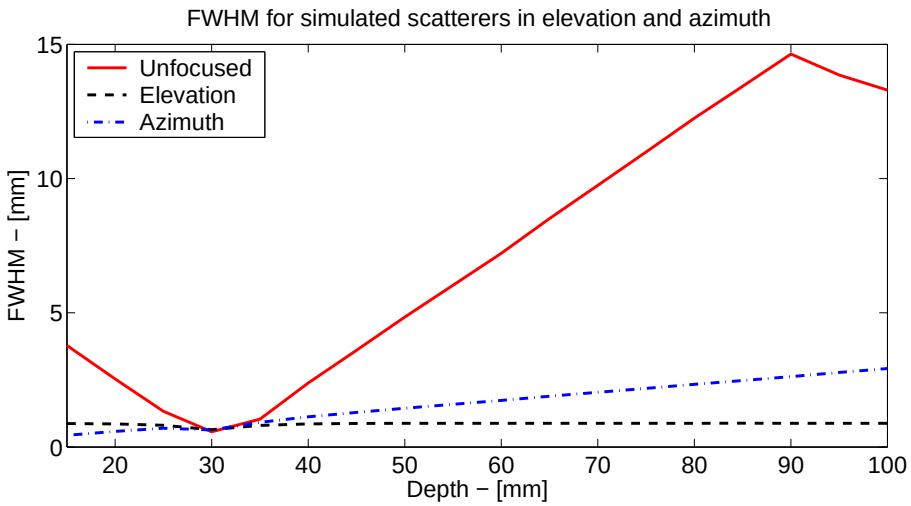

Figure 4.2: FWHM for simulated scatterers in elevation and azimuth as well as unfocused. The unfocused is assumed to be identical in both azimuth and elevation.

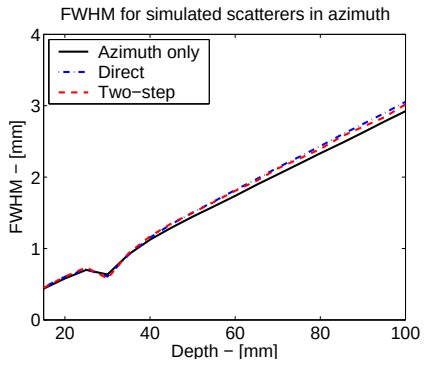

Figure 4.3: FWHM in azimuth for different focusing schemes. Single plane, spiral, and two-step SAF.

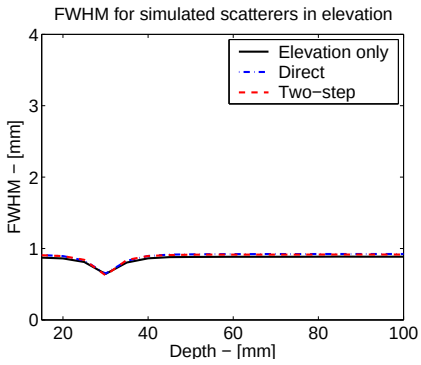

Figure 4.4: FWHM in elevation for different focusing schemes. Single plane, spiral, and two-step SAF.

side-lobe level was seen. Initial axial sampling density for the first step in the two-step method was chosen to be 1500 samples, basen on (2.5). In Fig. 4.5 it is shown how the sampling density influence the mean side-lobe level (MSLL). The initial sampling density is seen to be too sparse for the linear interpolation used at the second step. This requires either a higher axial sampling or a more advanced interpolation method [36]. At least 10,000 samples were required per line in the first beamforming step to reduce the side-lobe level for the two-step method to be comparable to the direct method, using linear interpolation.

4.2.2 Phantom Measurements

A validation of the performance of 3D SAF shown in simulations was done using a phantom containing speckle, wires, and cysts. The measurement was performed using a transducer and scanner system supplied by BK Medical Aps., Herlev, Denmark. The 3D SAF was performed using the two-step approach with 20,000 samples in the first step to assure a good result. Both 3D SAF methods gave comparable performance, and the direct method was less desirable when used on the linux cluster available at CFU.

The phantom contained all structures above the focus depth of the transducer, but performance

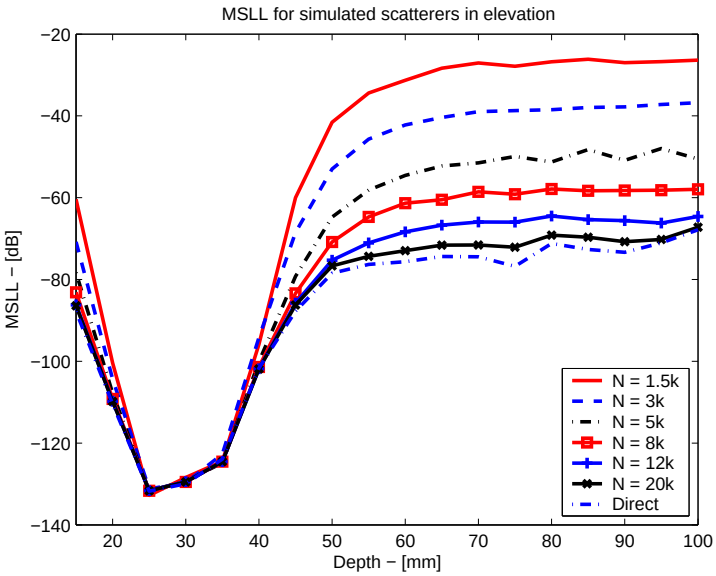

Figure 4.5: MSLL in elevation for different focusing schemes. Single plane, spiral, and two-step SAF.

is assumed to be comparable below the focus point as the waveform is often better behaved. The effect of applying 3D SAF is shown in Fig. 4.6 for the elevation plane and Fig. 4.7 for the azimuth direction. The center of rotation is placed at $(0, 0)$. Fig. 4.6 shows three wires in the elevation direction where the left image is the data as represented using the current system, and the right image is created using 3D SAF. Both scatterers and speckle are seen to be more uniform and depth independent when 3D SAF is applied. Scatterers in azimuth are shown in Fig. 4.7. As for the elevation image the speckle is shown much more homogeneous and the scatterers are much more clearly resolved. The scatterers at the top are 10 mm from the transducer, which allows for a significant improvement in performance. The image created using 3D SAF

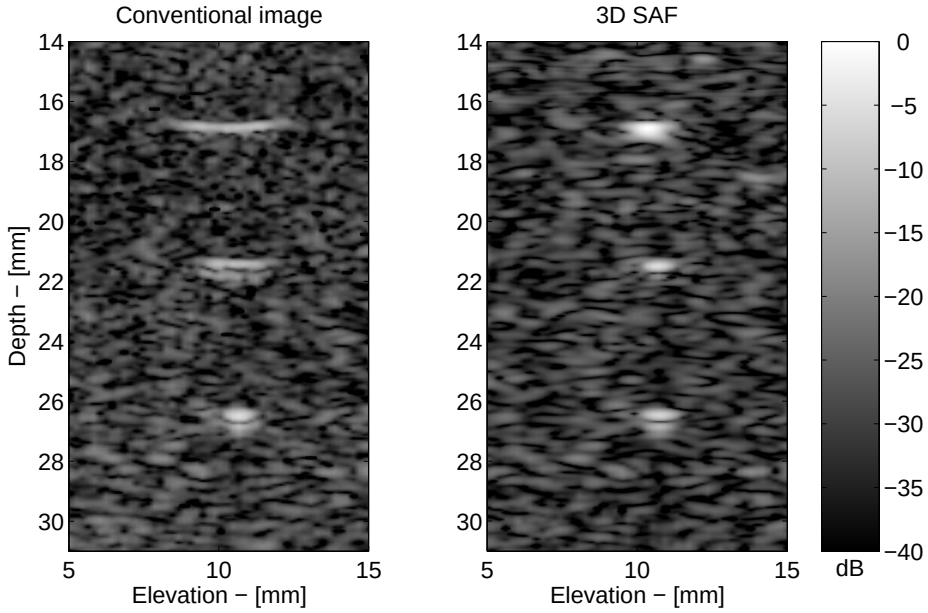

Figure 4.6: Comparison of three scatterers. The left image is created using conventional US imaging and the right is created by applying 3D SAF.

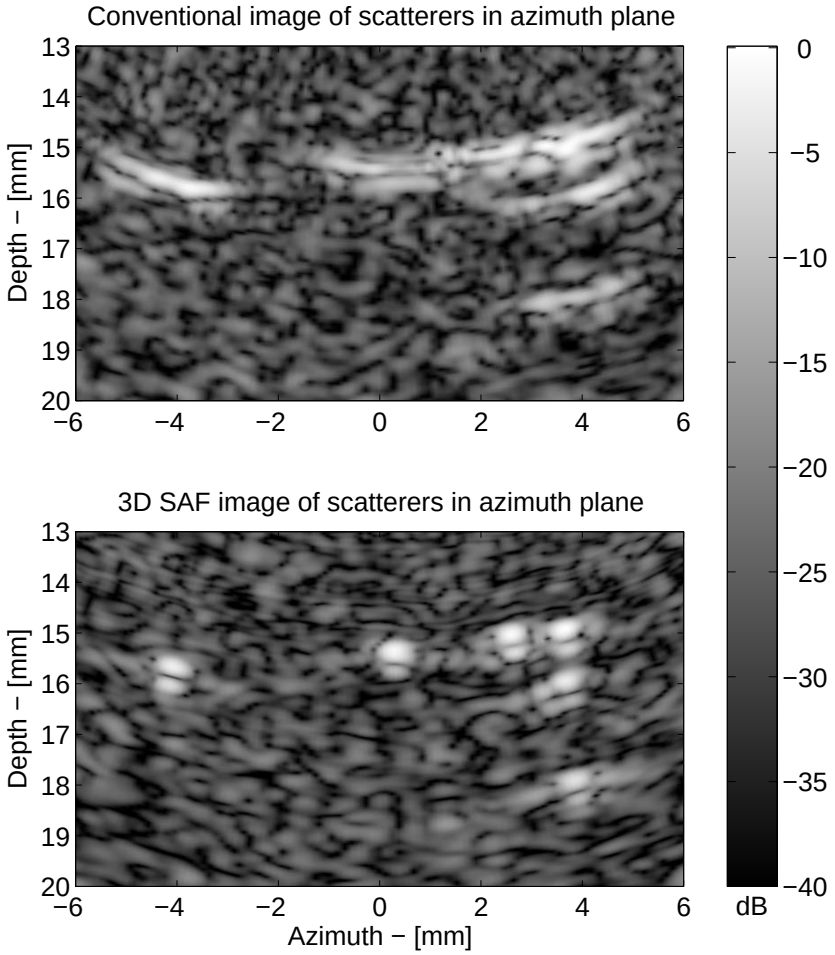

Figure 4.7: Several scatterers in azimuth with different distances and depths. The left image is created using conventional US imaging and the right is created by applying 3D SAF.

resolves all the scatterers where the conventional image has trouble resolving the structure of three closely lying scatterers. The ability to resolve close scatterers will improve functionality in e.g. relation to tracking and positioning of seeds during prostate cancer treatment. It has yet to be seen whether the method is able to reduce shadowing below seeds.

The gain SNR of the the two methods is estimated using (4.3) as well as using both a measured wire phantom and the speckle phantom. The wires in the wire-phantom are placed at 15 mm to 90 mm of depth with a 15 mm interval. To give a more smooth curve for the SNR estimate of the speckle part of the phantom, an averaged value is shown on the curve. All plots are shown in Fig. 4.8. The simulation show an in crease in SNR by 20 to 30 dB below the focal point, which would greatly increase the penetration depth of the transducer. The measurements only show a gain of $\approx$15 dB below the transducer focus, and almost no gain above the focus. The measurement estimate is assumed to be accurate since the gain in both speckle and wire measurements are very similar. All estimates show that an improvement in penetration will be possible with 3D SAF. This improvement can either increase imaging depth, or allow an increase in bandwidth for better image quality.

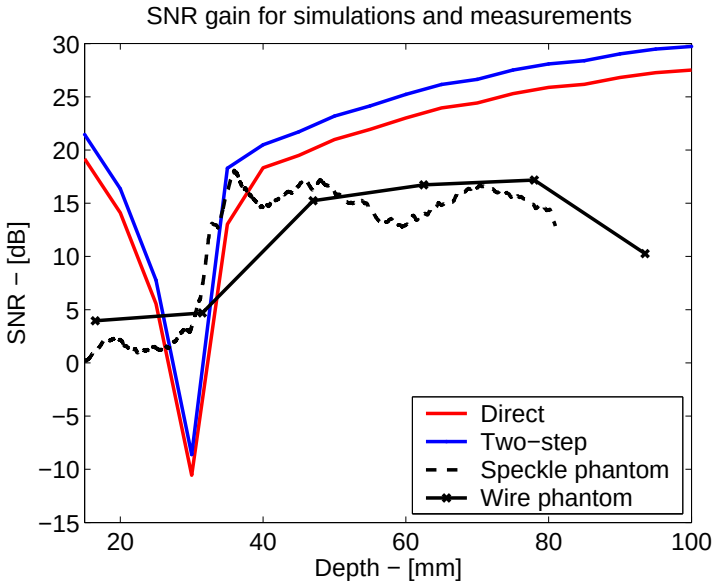

Figure 4.8: SNR increase by different SAF methods for simulated scatterers and measurements.

4.2.3 Processing

The two-step and direct SAF approach was shown to be able to perform almost with the same resolution and contrast. A comparison of the processing needed for each approach is made using the requirements for sampling density found in Fig. 4.5. To make the comparison simpler, only the number of lines, which each emission can contribute to, are estimated. The number of required points will then be the number of lines times the number of points per point. A line is assumed to be used if at least 1 point is within the acceptance angle of a given emission. This is shown in Fig. 4.9, where the solid lines show where the emission contribute down to the maximum depth used, indicated by the red dashed line.

The number of lines can be calculated analytically in both azimuth and elevation. In azimuth the quantity is given by

$$N_{\text{azi}}(z_{\text{max}}) = \frac{2}{d\theta} \arctan\left(\frac{\tilde{x}}{\tilde{z}}\right) + 1, \tag{4.5}$$

where $d\theta$ is the angular distance in azimuth between two emissions. $\tilde{x}$ and $\tilde{z}$ are given by

$$\tilde{x} = \frac{\sqrt{z_{\text{max}}^2 \gamma - z_{\text{vs}}} - 2F^{\#} z_{\text{vs}}}{\gamma} \tag{4.6}$$

$$\tilde{z} = 2F^{\#}\tilde{x} + z_{\text{vs}} \tag{4.7}$$

where z_{max} is the maximum depth required, z_{vs} is the depth of the virtual source used for beamforming, $F^{\#}$ is the f-number of the transducer$\gamma = 1 + (2F^{\#})^2$. The number of lines used for each emission in elevation is given by

$$N_{\text{ele}}(z_{\text{max}}) = \frac{|z_{\text{max}} - z_{\text{vs}}|}{F^{\#}\Delta y} + 1, \tag{4.8}$$

From (4.5) and (4.8) we can calculate the total number of points beamformed in each step of the two-step approach. For the direct approach, the number of lines used for each emission is

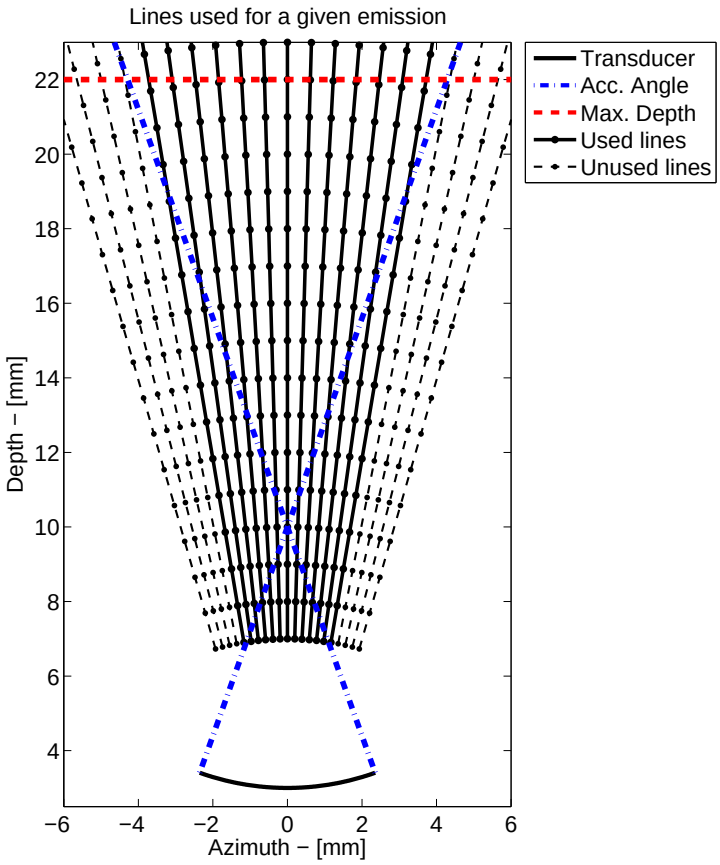

Figure 4.9: Visualization of the movement of a point relative to the transducer. The position of the virtual source is denoted r_{VS} and the rotation of the transducer is set at (0,0).

estimate by calculating the surface of an ellipse, where (4.5) and (4.8) defines the major and minor axis, giving the total number of lines used for each emission to

$$N_{\text{direct}}(z_{\text{max}}) = \pi N_{\text{ele}}(z_{\text{max}}) N_{\text{azi}}(z_{\text{max}}) \tag{4.9}$$

For an estimate of the total required number of beamformed points, the resulting volume is assumed to have 512 points per line and 900 lines per rotation. The two-step approach is set to have 12,000 samples per line to give side-lobes below -60 dB. The total required calculations for a given depth is shown in Fig. 4.10. This figure clearly shows that splitting beamforming in azimuth and elevation gives a reduction of around an order of magnitude. The two-step approach reduces the number of calculations, but requires an intermediate data-storage for the data after the azimuth focusing. This storage will equal the number of points beamformed, and the number of bytes is given by

$$B_{\text{storage}} = N_p N_l N_s B_d, \tag{4.10}$$

where N_p is the number of points per line, N_l is the number of lines, N_s is the number of elevation slices, and B_d is the bytes per point of data. For the setup used in this paper the total storage will be 9.07 GB of storage, assuming 16 bit complex data values and 210 slices of raw-data.

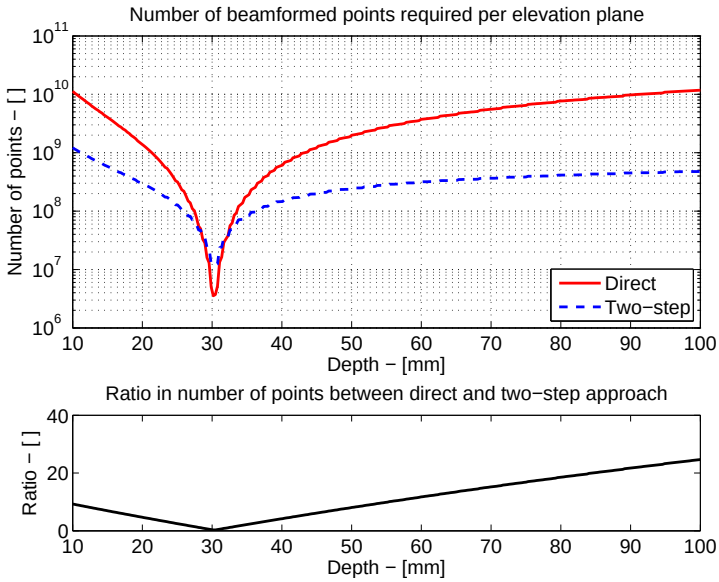

Figure 4.10: Number of points required to be processed per slice, assuming 900 lines per slice. The ratio between the two beamforming methods is shown at the bottom plot.

4.3 Conclusion

The results obtained using a single element transducer shows 3D SAF can be applied to a spiral scan with an improvement in both dimensions simultaneously, which is equal to the improvement obtained for each dimension independently. Applying 3D SAF also increases the SNR of at least 15 dB on the current system.

Both the direct and the two-step approach can perform equally well when resolution and side-lobe level are compared. The two-step approach has processing requirements that are more than an order of magnitude below the direct method, but requires a temporary storage of ≈4.5 GB to store the data from the first step. It has been shown that the processing demand on the two-step approach is directly related to the interpolation in the second step, and that improving the interpolation can reduce the required number of points in the first step.

CHAPTER

FIVE

Implementing 3D Synthetic Aperture Focusing

5.1 Interface and useability in total

Rocking arrays will give problems due to items mentioned in rocking array discussion

No ”magic” solution allowing a transducer which can be applied to a majority of places

TRUS arrays could benefit nicely due to motion being large, simple geometry, very nice interface to patient.

CHAPTER

SIX

Conclusion

Linear arrays for 3D imaging possible.

Problem will be using them for 2D, since no motion will be available.

Bibliography

[1] A. Fenster and D.B. Downey. Three-dimensional ultrasound imaging and its use in quantifying organ and pathology volumes. *Analytical and Bioanalytical Chemistry*, 377:982–989, 2003.

[2] R. G. Stock, N. N. Stone, M. F. Wesson, and J. K. DeWyngaert. A modified technique allowing interactive ultrasound-guided three-dimensional transperineal prostate implantation. *Int. J. of Radiation Oncology Biology Physics*, 32:219–225, 1995.

[3] G. Treece, R. Prager, A. Gee, and L. Berman. 3D ultrasound measurements of large organ volume. *Medical Image Analysis*, 5:41–54, 2001.

[4] R.M. Lang, V. Mor-Avi, L. Sugeng, P.S. Nieman, and D.J. Sahn. Three-dimensional echocardiography, the benefits of the additional dimension. *J. the American College of Cardiology*, 48(10):2053–2069, 2006.

[5] S. W. Smith, H. G. Pavy, and O. T. von Ramm. High-speed ultrasound volumetric imaging system – Part I: Transducer design and beam steering. *IEEE Trans. Ultrason., Ferroelec., Freq. Contr.*, 38:100–108, 1991.

[6] O. T. von Ramm, S. W. Smith, and Henry G. Pavy. High-speed ultrasound volumetric imaging system – Part II: Parallel processing and image display. *IEEE Trans. Ultrason., Ferroelec., Freq. Contr.*, 38:109–115, 1991.

[7] J. Kuo, G.R. Bredthauer, J.B. Castellucci, and O.T. Von Ramm. Interactive volume rendering of real-time three-dimensional ultrasound images. *IEEE Trans. Ultrason., Ferroelec., Freq. Contr.*, 54:313–318, 2003.

[8] L.J. Cutrona, E.N. Leith, L.J. Porcello, and W.E. Vivian. On the application of coherent optical processing techniques to synthetic-aperture radar. *IEEE Proc.*, 54:1026–1032, 1966.

[9] C. B. Burckhardt, P-A. Grandchamp, and H. Hoffmann. An experimental 2 MHz synthetic aperture sonar system intended for medical use. *IEEE Trans. Son. Ultrason.*, 21(1):1–6, January 1974.

[10] G. S. Kino, D. Corl, S. Bennett, and K. Peterson. Real time synthetic aperture imaging system. In *Proc. IEEE Ultrason. Symp.*, pages 722–731, 1980.

[11] K. Nagai. A new synthetic-aperture focusing method for ultrasonic *B*-scan imaging by the fourier transform. *IEEE Trans. Son. Ultrason.*, SU-32(4):531–536, 1985.

[12] K. Gammelmark. *Improving the Image Quality of Synthetic Transmit Aperture Ultrasound Images*. PhD thesis, Ørsted•DTU, Technical University of Denmark, 2800, Lyngby, Denmark, 2004.

[13] S. I. Nikolov. *Synthetic aperture tissue and flow ultrasound imaging*. PhD thesis, Ørsted•DTU, Technical University of Denmark, 2800, Lyngby, Denmark, 2001.

[14] J. J. Flaherty, K. R. Erikson, and V. M. Lund. Synthetic aperture ultrasound imaging systems, United States Patent, US 3,548,642, 1967, Published 22 Dec 1970.

[15] J. T. Ylitalo. Synthetic aperture ultrasound imaging using a convex array. In *Proc. IEEE Ultrason. Symp.*, pages 1337–1340, 1995.

[16] M. Karaman, P. C. Li, and M. O'Donnell. Synthetic aperture imaging for small scale systems. *IEEE Trans. Ultrason., Ferroelec., Freq. Contr.*, 42:429–442, 1995.

[17] M. H. Pedersen, K. L. Gammelmark, and J. A. Jensen. Preliminary in-vivo evaluation of convex array synthetic aperture imaging. In *Proc. SPIE - Progress in biomedical optics and imaging*, pages 33–43, 2004.

[18] J. T. Ylitalo and H. Ermert. Ultrasound synthetic aperture imaging: monostatic approach. *IEEE Trans. Ultrason., Ferroelec., Freq. Contr.*, 41:333–339, 1994.

[19] C. Passmann and H. Ermert. In vivo imaging of the skin in the 100 mhz region using the synthetic aperture concept. *Proc. IEEE Ultrason. Symp.*, 2:1287–1290, 1995.

[20] S. I. Nikolov, K. Gammelmark, and J. A. Jensen. Recursive ultrasound imaging. In *Proc. IEEE Ultrason. Symp.*, volume 2, pages 1621–1625, 1999.

[21] J. A. Jensen and S. I. Nikolov. Directional synthetic aperture flow imaging. *IEEE Trans. Ultrason., Ferroelec., Freq. Contr.*, 51:1107–1118, 2004.

[22] N. Oddershede, L. Løvstakken, H. Torp, and J. A. Jensen. Estimating 2-d vector velocities using multidimensional spectrum analysis. *IEEE Trans. Ultrason., Ferroelec., Freq. Contr.*, 55(8):1744–1754, 2008.

[23] S. I. Nikolov and J. A. Jensen. Virtual ultrasound sources in high-resolution ultrasound imaging. In *Proc. SPIE - Progress in biomedical optics and imaging*, volume 3, pages 395–405, 2002.

[24] N. Oddershede and J. A. Jensen. Effects influencing focusing in synthetic aperture vector flow imaging. *IEEE Trans. Ultrason., Ferroelec., Freq. Contr.*, 54:1811–1825, 2007.

[25] J. T. Ylitalo. On the signal-to-noise ratio of a synthetic aperture ultrasound imaging method. *Eur. J. Ultrasound*, 3:277–281, 1996.

[26] J. T. Ylitalo. Improving contrast resolution in ultrasound holographic B-imaging: comparison between simulation and experiment. In *Proc. IEEE Ultrason. Symp.*, pages 1011–1014, 1993.

[27] M. H. Bae, M. K. Jeong, T. K. Song, and Y. B. Ahn. Experimental study of transmit synthetic focusing combined with receive dynamic focusing in B-mode ultrasound imaging systems. In *Proc. IEEE Ultrason. Symp.*, pages 1261–1264, 1999.

[28] M. H. Bae and M. K. Jeong. A study of synthetic-aperture imaging with virtual source elements in B-mode ultrasound imaging systems. In *IEEE Trans. Ultrason., Ferroelec., Freq. Contr.*, volume 47, pages 1510–1519, 2000.

[29] C. Passmann and H. Ermert. A 100-MHz ultrasound imaging system for dermatologic and ophthalmologic diagnostics. *IEEE Trans. Ultrason., Ferroelec., Freq. Contr.*, 43:545–552, 1996.

[30] C. H. Frazier and W. D. O'Brien. Synthetic aperture techniques with a virtual source element. *IEEE Trans. Ultrason., Ferroelec., Freq. Contr.*, 45:196–207, 1998.

[31] G. R. Lockwood, J. R. Talman, and S. S. Brunke. Real-time 3-D ultrasound imaging using sparse synthetic aperture beamforming. *IEEE Trans. Ultrason., Ferroelec., Freq. Contr.*, 45:980–988, 1998.

[32] S. I. Nikolov and J. A. Jensen. Application of different spatial sampling patterns for sparse array transducer design. *Ultrasonics*, 37(10):667–671, 2000.

[33] R. T. Hoctor and S. A. Kassam. The unifying role of the coarray in aperture synthesis for coherent and incoherent imaging. In *IEEE Proc.*, volume 78, pages 735–752, 1990.

[34] S. I. Nikolov, P. Santén, O. Bjuvsten, and J. A. Jensen. Parameter study of 3D synthetic aperture post-beamforming procedure. *Ultrasonics*, 44:e159–e164, 2006.

[35] J. Kortbek, J. A. Jensen, and K. L. Gammelmark. Synthetic aperture sequential beamforming. In *Proc. IEEE Ultrason. Symp.*, pages 966–969, 2008.

[36] J. Kortbek, H. Andresen, S. Nikolov, and J. A. Jensen. Comparing interpolation schemes in dynamic receive ultrasound beamforming. In *Proc. IEEE Ultrason. Symp.*, pages 1972–1975, 2005.

[37] J. A. Jensen, O. Holm, L. J. Jensen, H. Bendsen, S. I. Nikolov, B. G. Tomov, P. Munk, M. Hansen, K. Salomonsen, J. Hansen, K. Gormsen, H. M. Pedersen, and K. L. Gammelmark. Ultrasound research scanner for real-time synthetic aperture image acquisition. *IEEE Trans. Ultrason., Ferroelec., Freq. Contr.*, 52 (5):881–891, May 2005.

[38] G. R. Lockwood and F.S. Foster. Design of sparse array imaging systems. In *Proc. IEEE Ultrason. Symp.*, pages 1237–1243, 1995.

[39] K. Kawabe, Y. Hara, K. Watanabe, and T. Shimura. An ultrasonic transducer apodization by polarization. In *Proc. IEEE Ultrason. Symp.*, volume 2, pages 809–813, 1990.

[40] J. N. C. Chen, G. G. Vogel, and M. K. Mason. Ultrasonic transducer apodization using acoustic blocking layer, US Patent 5,285,789, Priority date: 1992, Granted 1994.

[41] M. P. Finsterwald. Ultrasonic transducer array with apodized elevation focus, International Patent WO 96/11753, Priority date: 1995, Granted 1996.

[42] FDA. Information for manufacturers seeking marketing clearance of diagnostic ultrasound systems and transducers. Technical report, Center for Devices and Radiological Health, United States Food and Drug Administration, 1997.

[43] J. Kortbek, J. A. Jensen, and K. L. Gammelmark. Synthetic Aperture Focusing Applied to Imaging Using a Rotating Single Element Transducer. In *Proc. IEEE Ultrason. Symp.*, pages 1504–1507, Oct. 2007 (Accepted).

[44] A. Fenster, S. Tong, H.N. Cardinal, C. Blake, and D.B. Downey. Three-dimensional ultrasound imaging system for prostate cancer diagnosis and treatment. *IEEE Trans. Instrumentation and Measurements*, 47:1439–1447, 2003.

[45] F. N. Ucar and Mustafa Karaman. Beam space processing for low-cost scanners. In *Proc. IEEE Ultrason. Symp.*, pages 1349–1352, 1996.

APPENDIX

A

Precise Time-of-Flight Calculation for 3D Synthetic Aperture Focusing

Paper describing the a new time-of-flight calculation for 3D SAF. The paper has been accepted for publication in IEEE UFFC.

A.1 Precise Time-of-Flight Calculation for 3D Synthetic Aperture Focusing - Conference Paper

APPENDIX

B

Rocking Convex Array used for 3D Synthetic Aperture Focusing

B.1 Rocking Convex Array used for 3D Synthetic Aperture Focusing - Conference Paper

APPENDIX

C

Spiral Motion Single Element Transducer

APPENDIX

D

Cardiac In-Vivo Measurements using SAF

APPENDIX

E

Visualization

Rendering or edge-rendering, ray-tracing, slice-intersections

Visualization techniques. What is used at BK-Medical, and what are they doing at Duke.

Dedicated hardware, shaders, real-time scan-conversion. Work done at Duke, show simple model of 3D flow value.

APPENDIX

F

Fast Beamformation Toolbox

Legacy beamformation toolbox

Improvements using Duke knowledge and Nikolov paper.

Speed improvements beamforming simple SAF image of 1k-by-1k.

APPENDIX

G

Derivations

This section contains derivations used in the thesis and the papers, but which is not essential for reading and understanding the thesis.

G.1 Estimate of Gain in Signal-to-Noise Ratio

Calculating the signal-to-noise ratio (SNR) is often done using repeated measurements. Having a moving transducer makes repeated measurements difficult to obtain, and an alternative method for calculating a change in SNR is made. The change is calculated between a signal obtained using SAF and a signal with no focusing. The gain in signal SNR at time t is given by

$$\text{SNR}_{\text{gain}}(t) = \frac{\text{SNR}_{\text{sa}}(t)}{\text{SNR}_{\text{uf}}(t)} = \frac{\left(\frac{P_{\text{sa}}(t)}{P_{\text{uf}}(t)}\right)}{\left(\frac{P_{\text{noise,sa}}(t)}{P_{\text{noise,uf}}(t)}\right)}, \tag{G.1}$$

where P_{sa} is the power of the synthetic aperture signal, P_{uf} is the power of the unfocused signal, $P_{\text{noise,sa}}$ is the noise power of the synthetic aperture signal, and $P_{\text{noise,uf}}$ is the noise power of the unfocused signal.

The basic assumption will be that the amplitude of the tissue is dominated by signal, which makes the method valid in the region with high SNR and less valid where the SNR drops. This allows the method to give a good estimate for simulations where the signal amplitude is exactly known, where measurements have varying degree of certainty. With this assumption, two equations for the SAF and unfocused signal power

$$P_{\text{sa}}(t) = p_{\text{sa}}^2(t) = \left(\sum_{j=1}^{J} p_j(t) a_j(t)\right)^2 \tag{G.2}$$

$$P_{\text{uf}}(t) = p^2(t), \tag{G.3}$$

where $g_j(t)$ is the signals summed when applying SAF focusing, $a_j(t)$ is the apodization of the j'th signal at time t, J is the number of used signals in SAF, and $g(t)$ is the unfocused signal. Assuming

The noise power is given by

$$P_{\text{noise,sa}}(t) = E\left[\left(\sum_{j=1}^{J} n_j(t)a_j(t)\right)^2\right] \tag{G.4}$$

$$P_{\text{noise,uf}}(t) = E[n^2(t)], \tag{G.5}$$

where $E[\dot{]}$ is the expectation value, $n_j(t)$ is the noise part of the j'th signal, and $n(t)$ is the noise part of the unfocused signal. Assuming uncorrelated white noise with zero mean allows (G.5) to be written as $E[n^2(t)] = \sigma_n^2(t)$. The noise power changes with time because of a change in the receive gain of the system. It is assumed that the noise is dominated by electronic noise, and that it can be assumed to be quasi-stationary in a short duration in time. This allows (G.4) to be rewritten using $\sigma_{n,j}^2(t) = \sigma_n^2(t)a_j^2(t)$ which gives

$$P_{\text{noise,sa}}(t) = \sum_{j=1}^{J} \sigma_{n,j}^2(t) = \sigma_n^2(t) \sum_{j=1}^{J} a_j^2(t), \tag{G.6}$$

This allows a combination of (G.2), (G.3), (G.5), and (G.6) with the original (G.1), giving

$$\text{SNR}_{\text{gain}}(t) = \frac{p_{\text{sa}}^2(t)}{p^2(t)\sum_{j=1}^{J} a_j^2(t)} \tag{G.7}$$

APPENDIX

H

Images

This chapter contains images omitted from the thesis text.

H.1 Rocking Convex Array Transducer

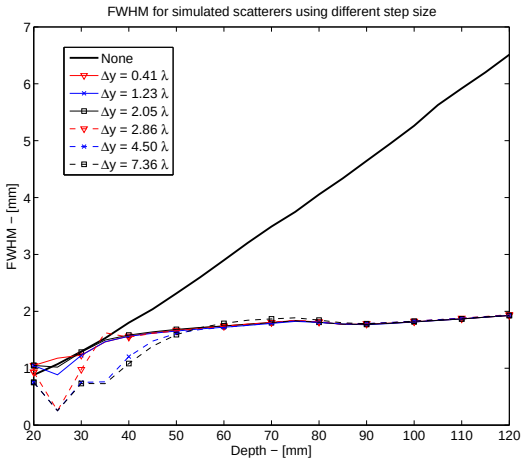

Figure H.1: Image of the rocking array transducer.